Summer 2019

Mesoscale Controls on the Shasta County Convergence Zone

Matthew Thomas Roberts
San Jose State University

MESOSCALE CONTROLS ON THE SHASTA COUNTY CONVERGENCE ZONE

A Thesis

Presented to

The Faculty of the Department of Meteorology and Climate Science

San José State University

In Partial Fulfillment

of the Requirements for the Degree

Master of Science

by

Matthew T. Roberts

August 2019

The Designated Thesis Committee Approves the Thesis Titled

MESOSCALE CONTROLS ON THE SHASTA COUNTY CONVERGENCE ZONE

by

Matthew T. Roberts

APPROVED FOR THE DEPARTMENT OF METEOROLOGY AND CLIMATE SCIENCE

SAN JOSÉ STATE UNIVERSITY

August 2019

Craig Clements, Ph.D.	Department of Meteorology and Climate Science
Sen Chiao, Ph.D.	Department of Meteorology and Climate Science
Neil Lareau, Ph.D.	University of Nevada, Reno, Department of Atmospheric Science

ABSTRACT

MESOSCALE CONTROLS ON THE SHASTA COUNTY CONVERGENCE ZONE

Matthew T. Roberts

The Shasta County Convergence Zone (SCCZ) is a poorly understood terrain-forced convergence zone that develops at the northern terminus of California's Sacramento Valley during cool season (Oct.-Apr.) trough passages. While terrain-flow interactions clearly factor into the SCCZ development, the nature of these interactions is unknown as are the mesoscale processes affecting event duration and orientation. Level-II NEXRAD radar data are used to examine the onset, duration, orientation, geographical extent, and precipitation rate of 23 SCCZ events during the 2016-2017 cool season. The analyses reveal distinct event morphologies including (1) isolated convective bands over the topography, (2) isolated convective bands displaced off of the topography over the Sacramento Valley, and (3) linear convective bands embedded within broader regional precipitation. Event duration ranges from 1 hour to more than 9 hours, and single event estimated rainfall is as high as 100 mm in some locations. Additionally, RAP model analyses, WRF simulations and in situ observations are used to investigate stability parameters and vertical wind and moisture profiles between different cases. These data indicate that location of convective bands is dependent on wind speed and direction in the low and middle levels of the atmosphere. Linearity and orientation of convective lines appear to be linked to the low level shear profile and mean winds. The non-dimensional mountain height is also examined as a control parameter, showing some utility in distinguishing between convective initiation locations.

ACKNOWLEDGEMENTS

First and foremost, I would like to thank my advisor Dr. Neil Lareau for his insight, motivation and patience throughout the research process. This research would not be the same without his guidance. Second, I would like to acknowledge Drs. Craig Clements and Sen Chiao for serving on my thesis committee and providing invaluable feedback on my work. I would also like to thank the faculty and my colleagues in the SJSU department of meteorology for their support.

Lastly, I would like to thank my friends and family for their motivation and support during my time at SJSU. Special thanks to my girlfriend Alexis for her constant encouragement despite the moments of grumpiness, stress and long nights that came with completing this research. Finally, I can't forget an important thank you to my parents for their support throughout my life.

TABLE OF CONTENTS

LIST OF TABLES

LIST OF FIGURES

1. Introduction

While terrain-forced convergence and its role in convective initiation have been studied extensively across the western United States (Mass 1981; Wesley et al. 1995; Andretta and Hazen 1997; Alcott and Steenburgh 2013), there is a striking lack of literature examining a unique, high-impact, terrain-forced region of convective initiation in the northern Sacramento Valley (NSV) of California. This region is characterized by consistent convective precipitation bands that develop during the California wet season (October-April). There are a number of factors that make this region unique, namely the persistence, longevity and linear organization of the convective bands. It is believed that the complex topography surrounding the NSV plays an important role in the development of convection through terrain forced convergence of flow in the NSV. For this reason local National Weather Service and television meteorologists have established the name: "Shasta County Convergence Zone" (SCCZ), named after the county in the NSV where convection most often initiates during these events (Fig. 1).

The SCCZ generally refers to the area between Redding (KRDD) and Shasta Lake (SHDC1), located at the northern terminus of the NSV. The SCCZ is surrounded by topography on 3 sides. The Yolla Bolly Mountains rise approximately 2400 meters above mean sea level (MSL) to the southwest of the area, in western Tehama and southern Trinity Counties. The Trinity Alps cover the regions west and northwest of the SCCZ, at elevations of 2000-2700 meters above MSL in northern Trinity and southern Siskiyou Counties. The Trinity Mountains comprise the region between the Trinity Alps and the city of Redding. In this study, we further divide the Trinity Mountains into upper (west

and northwest of Shasta Lake; 500-1500 meters above MSL) and lower (south and southwest of Shasta Lake; <600 meters above MSL) regions. The southern edge of the Cascades marks the northern boundary of the SCCZ at approximately 1500 meters above MSL. To the northeast lies the far western portion of the Great Basin, about 1200 meters above MSL. To the east-southeast lies the northern fringe of the Sierra Nevada at elevations of 1500 to 3000 meters above MSL. To the south is the low lying Sacramento Valley, gradually declining in elevation from approximately 200 meters above MSL in Redding to near sea level in Sacramento (KSAC).

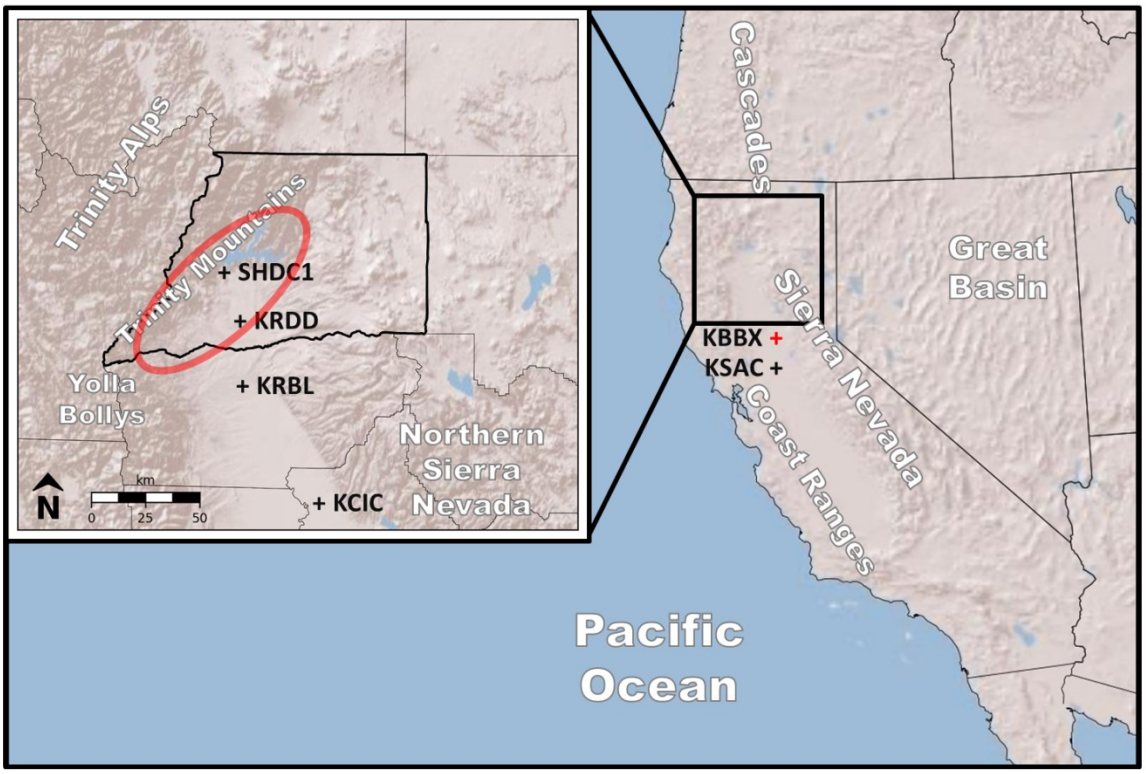

Fig. 1. SCCZ highlighted in red with significant topographic barriers surrounding the region labeled in white. Shasta County is outlined in black. Surface meteorological observation sites are labeled and indicated with a black cross. KBBX radar location is indicated with a red cross.

Precipitation in this region presents several significant societal impacts due to the close proximity to population centers (Shasta Lake, Redding, Red Bluff), transportation corridors (Interstate 5, State highways 299 and 44), and outdoor recreation and water resources (Shasta Lake). Shasta Lake is of particular importance due to its ranking as the highest capacity reservoir in California, with a storage capacity just over 4.5 million acre-feet (Graf 2006). Shasta Lake is not only important for water storage in the state of California. The meteorological station at Shasta Dam is also a part of the Northern Sierra 8-station index; a climatological benchmark for precipitation and snowpack health in northern California. SCCZ events influence precipitation and associated runoff into Shasta Lake multiple times every year. Additionally, during the 2016-17 wet season alone multiple SCCZ precipitation events induced flash flooding and mudslides, forcing closures of major highways in the region. Recent wildfires in the region (e.g., the Carr, Hirz, and Delta Fires) further compound the risk of debris flows and flash flooding associated with the SCCZ. These potential impacts to society, infrastructure and water resources necessitate a better understanding of the mechanisms driving convection in the SCCZ.

Previous hydroclimate research in the region has documented the precipitation effects of large scale orographic lift and blocking, resulting in the Sierra barrier jet, which is a south-north low level jet that develops due to ridging and flow blocking along the windward slopes of the Sierra Nevada (Parish 1982). Further studies (e.g. Hughes et al. 2012; Neiman et al. 2014; Ralph et al. 2016) have established that significant orographic precipitation occurs over the Trinity Alps and Shasta County Mountains as a result of the

Sierra barrier jet; however the details of the organization of these events have not been established. Montevardi (1994) and Staudenmaier (1995) noted that the Central Valley region as a whole is sometimes conducive to strong thunderstorms. Additionally, Tardy (2002) cataloged convective events during the October-May period from 1999 to 2001, noting the presence of a surface convergence zone in the NSV. However, no comprehensive and quantitative study has been conducted specifically on the unique mesoscale convective processes in the SCCZ. Therefore, the goals of this research are: (1) broadly determine the background synoptic requirements necessary to initiate convection over the SCCZ, (2) identify the finer scale processes that dictate whether convection initiates over topography near Shasta Lake, or upstream of topography near Redding, and furthermore (3) diagnose the dominant factors that organize SCCZ convective events into long-lived squall lines or shorter lived disorganized convection.

2. Background

Topography can be an important mechanism for initiating moist convection via mechanical and thermal forcing. The most well-known mechanical mechanisms for convective initiation are forced ascent along mountain slopes and dynamically forced convergence upstream and downstream of mountain barriers (Banta 1990; Kirshbaum et al. 2018). The strength and location of ascent can be sensitive to a number of variables including: wind direction and speed (Mass 1981; Andretta and Hazen 1997), atmospheric stability (Houze et al. 2001), shape and orientation of surrounding orography (Hagen et al. 2011; Watson and Lane 2012) and moisture availability (Hagen et al. 2011). Gaining a better understanding of the interaction amongst these processes aids in predicting where

moist convection initiates, its subsequent intensity, and potential regions of cloudiness and precipitation. However, the mesoscale controls of orographic convection are difficult to generalize, often varying due to the specifics of regional topography and the thermodynamic structure of the atmosphere. These inconsistencies have led to limitations in the understanding of processes important to forecasting convection, most notably convective preconditioning and initiation (Kirshbaum et al. 2018).

While orographic convection and terrain forced convergence are distinctly mesoscale phenomena, they remain forced by the overlying synoptic conditions. Mass (1981) noted this relationship in the Puget Sound convergence zone (PSCZ) of western Washington State. Synoptic scale pressure gradients dictate the intensity and direction of winds along the Washington coast, ultimately determining whether the flow is susceptible to topographic channeling through the Strait of Juan de Fuca and Chehalis Gap north and south of the Olympic Mountains. Generally PSCZ events correlate with a frontal passage over coastal Washington leading to west-northwest surface winds. This flow regime combined with at least some stability (e. g. Froude numbers <1) supports flow splitting around the Olympic Mountains and converging on the lee side, often resulting in enhanced cloudiness and precipitation.

Similar synoptic flow dependencies are noted by Andretta and Hazen (1997) in their study of a convergence over the Snake River Plain (SRP) of southeast Idaho. Convergence over the SRP is characterized as a mesoscale feature in terrain channeled boundary layer flow, the occurrence of which is highly sensitive to the background synoptic conditions. Specifically, the SRP typically develops post-frontal flow as winds

in the lower troposphere shift to northwesterly over southern Idaho. These conditions lead to convergence near the northeast terminus of the Snake River Valley, which subsequently initiates virga producing cloud bands and occasional moderate to heavy precipitation.

The sensitivity of orographic precipitation to wind speed, stability, and barrier height has also been examined by Houze et al. (2001) in a radar-based study of moist orographic ascent over the Alps. These factors can be succinctly represented in the Froude number (Fr), defined as:

$$Fr = \frac{U}{NH} \tag{1}$$

Where H is the height of the mountain barrier, U is the mean (surface to H) upstream flow speed, and N is the Brunt Väisälä frequency,

$$N = \sqrt{\frac{g}{\theta}\frac{\partial \theta}{\partial z}} \tag{2}$$

and θ is the potential temperature. Fr is a good indicator whether flow will rise over or become blocked by a topographic barrier (Durran 1990; Houze 1993), though it is sometimes difficult to apply to real world situations. Houze et al. (2001) found correlations between accumulated precipitation and the speed and direction of flow impinging on the Alps, noting that high Fr flow (Fr > 1) easily rises over terrain and enhances precipitation over windward slopes whereas low Fr flow (Fr < 1) tends to experience terrain blocking and precipitation enhancement upstream of the topography. These results are consistent with the findings of Grossman and Durran (1984) that the location of precipitation maxima varied between high and low Fr flows and the results of

Mass and Dempsey (1985) showing that low Fr flow was key in developing the deflected flow necessary to initiate the PSCZ.

These stability, flow, and terrain sensitivities can also be expressed as the "non-dimensional mountain height" (M), which is simply the inverse of the Froude number (Kirshbaum et al. 2018), defined as:

$$M = \frac{NH}{U} \tag{3}$$

Specifically, $M > 1$ leads to flow blocking, $1 < M < 2$ leads to stagnant or reversed flow in the lee of the barrier, and $M \leq 1$ allows air to ascend mountain barriers unblocked. The non-dimensional mountain height is sometimes considered preferable to the Froude number since the Froude number has other specific, dynamical interpretations pertaining to wave propagation. Regardless, either the Froude number or the non-dimensional mountain height contain the same information about flow blocking.

Hagen (2011) examined the Fr dependence of convective initiation during the Convective and Orographically-induced Precipitation Study (COPS) field campaign in Central Europe. Specifically, COPS examined thermally driven convection over a few isolated mountain ridges. They found that under low Fr conditions winds were deflected around the topography and thermally driven convergence along the mountain ridges initiated convection. Conversely, when Fr conditions were high, flow passed through gaps in the mountains and converged in the leeside valley initiating convection that was displaced from the topography. In their cases, variations in the Froude number were dominated by variations in the flow speed: low Fr flows corresponded with weak winds

varying with height, whereas high Fr flows exhibited strong winds that increased with height. They also noted that orientation of the topography was an important factor in determining locations of convection. The link between channeling of winds between mountain passes and leeside convection suggested that convergence was more likely to occur where wind aligned passes and gaps entered the adjacent valley.

The sensitivity of precipitation distributions to the shape and orientation of topography relative to the prevailing flow was further examined by Watson and Lane (2012). Using idealized simulations with differing mountain ridge shapes (linear, concave and convex) but a fixed non-dimensional mountain height of unity, they found distinct precipitation distributions due to the effects of confluence, deflection, deceleration, and channeling of the flow. Concave ridges produced the greatest precipitation maxima, consistent with the results of Jiang (2006), and even subtle changes to the terrain geometry were found to impact precipitation location and intensity. Similar sensitivities were also observed by Anders et al. (2007) in observations over the Olympic Mountains of Washington State.

The sensitivities to orography and flow variations have also been examined by Alcott and Steenburgh (2013) over the Great Salt Lake (GSL) and adjacent Wasatch Range of northern Utah. Three primary orographic influences on GSL convergence were identified. First, down sloping flow over upstream orography dried and warmed the air mass, ultimately shifting the location and extent of the GSL effect precipitation band. Second, blocking and channeling of flow by upstream orography enhanced downstream convergence over the GSL, affecting the evolution and structure of the precipitation

band; results that are similar to conclusions from Mass (1981) and Mass and Dempsey (1985). Finally, blocking and channeling of flow by downstream orography further enhances GSL convergence resulting in enhanced precipitation. Although this study focused on lake-effect processes it further emphasizes the impacts complex topography can have on a pre-existing convergence zone.

In addition to terrain forced convergence, one common feature often found in mountainous regions, including the SCCZ, is quasi-stationary, linear precipitation bands. These bands can take different forms and vary in structure and location. Yoshizaki et al. (2000), for example, noted the presence of isolated, linear, quasi-stationary bands downstream of topography in the Kyushu region of Japan. The most persistent bands lasted nearly 24 hours and produced localized precipitation enhancements up to 30 cm. Similar convective orographic rain bands have been identified near Cèvennes, France (Miniscloux et al. 2001). However, these bands differ from those in Japan in that they occur embedded in larger scale precipitation over the region rather than discrete bands. These findings are notable in that both isolated bands and bands embedded within background precipitation have been observed over the SCCZ, as we show later.

Persistent orographic precipitation bands over the Coastal Ranges of Oregon (north and west of the SCCZ) have also been identified (Kirshbaum and Durran 2005b). These bands exhibit greater temporal coherence than those studied by Yoshizaki et al. (2000) and Miniscloux et al. (2001). Kirshbaum and Durran (2004, 2005a) and Yoshizaki et al. (2000) indicate that vertical wind shear strongly influences band development, though Cosma et al. (2002) found that bands can also form in the absence of vertical wind shear.

For sheared cases, there is some uncertainty in whether the mean wind or shear vector is responsible for the orientation of the bands. Cosma et al. (2002) and Miniscloux et al. (2001) found, for example, that orographic rain bands organize parallel to the mean flow vectors, whereas Yoshizaki et al. (2000) found that bands appear to organize parallel to the shear vectors. Interestingly, Kirshbaum and Durran (2005a) found evidence of both, sometimes occurring simultaneously.

To probe sensitivities in convective initiation and organization Kirshbaum and Durran (2005b) performed idealized simulations with variations in terrain roughness, heterogeneity of the background thermal fields, and the magnitude of the shear. They found that bands commonly result from several atmospheric parameters superimposed on one another. For example, the interaction amongst dry stability, moist instability, wind shear, thermal fluctuations, and terrain roughness often determines the degree of "bandedness", orientation, and overall organization found in the simulations. Despite these complex interactions, they conclude that quasi-stationary linear convective bands require two key components: 1) moist instability or potential instability, with strong dry stability in the lower troposphere region that is lifted over topography and 2) strong unidirectional wind shear through the moist layer. More specifically, the strength and direction of the vertical wind shear strongly influences whether bands orient with the mean flow or along the shear vector. Flows with unidirectional wind shear and marginal instability produced well defined bands; however only bands initiated due to small perturbations in the topography remained stationary, while thermally initiated bands were more transient. Conversely, directional wind shear tended to degrade band organization,

as wind shear generated shear parallel bands that suppressed the flow parallel bands.

Additionally, during favorable winds stationary, flow parallel bands developed as a result of lee waves formed from stable flow moving over roughened topography upstream of the orographic clouds. These bands were more resilient to influences of directional wind shear, and when superimposed upon unidirectional shear environments and topographically initiated convection, produced more robust stationary rain bands. As we will see, many of these same components are at play in the organization of the SCCZ.

3. Methodology

a. Radar Data

SCCZ events are identified using the Next Generation Weather Surveillance Radar-1988D (NEXRAD WSR-1988D) network, which provides operational radar coverage across most of the contiguous United States (Crum et al. 1993). While complex terrain can impede radar coverage in parts of the western US (Matrosov et al. 2014), the Beale Air Force Base (KBBX) WSR-88D site provides reliable spatio-temporal observations of precipitation features in and around the SCCZ. KBBX is situated approximately 150 km south-southeast of the SCCZ near the city of Oroville, California (Fig. 1) and generates a volume coverage pattern (VCP) composed of successive 360° azimuthal plan position indicator (PPI) scans every four to ten minutes. This study only uses the 0.5° elevation angle PPI to identify precipitation in the SCCZ. The radar scans have a range gate length of 250 m and are spaced in 0.5° azimuthal increments. The total range is 230 km from the radar tower (Federal Meteorological Handbook, no. 11). Due to distance and Earth's curvature, the center of the radar beam is approximately 2700 m above ground level in

the vicinity of the SCCZ with a resolution of 250 m between range gates and 1309 m between adjacent azimuth steps.

Precipitating days over the SCCZ were identified over the course of the 2016-17 wet season (October-April). KBBX level II NEXRAD data were obtained through the National Center for Environmental Information (NCEI) for the identified days (Crum et al. 1993). The data were manually analyzed to find persistent, quasi-linear and quasi-stationary convective bands in the NSV. Initiation times were identified using the first persistent convective reflectivity echoes exceeding 20 dBZ in the region of the SCCZ. Cessation was identified as the time when 20 dBZ cells dissipated, lost their convective characteristics, or transited out of the NSV. Additionally, initiation and cessation locations were categorized as occurring over the Trinity Mountains west and north of the NSV (terrain initiation/cessation), or within the NSV itself (valley initiation/cessation). This stratification of the data is utilized later to probe the processes contributing to different types of SCCZ events. In all, 23 events were identified during the study period with durations ranging from 1.5 hours to more than 13 hours (See Table 1).

Table 1. Dates of SCCZ events from October 2016 through April 2017, initiation and cessation times rounded to the nearest 5-minute interval, event duration, initiation and cessation locations, where T and V indicate Terrain and Valley, respectively.

Date	Initiation Time (PST)	Cessation Time (PST)	Duration (HH:MM)	Maximum Radar Est. Precipitation (mm)	Initiation Point (T/V)	Cessation Point (T/V)
18-Apr	2030	0200	05:30	25	T	T
12-Apr	1245	1620	03:35	40	T	T
7-Apr	0445	1830	13:45	45	T	V
22-Mar	0550	1440	08:50	45	V	V
21-Mar	1030	1550	05:10	35	T	T
4-Mar	1230	0300	14:30	50	V	V
21-Feb	1500	2030	05:30	45	V	V
18-Feb	1530	2230	07:00	30	V	V
16-Feb	1115	1340	02:25	20	V	V
9-Feb	1230	2045	08:15	55	T	V
8-Feb	1600	2225	06:25	55	T	T
22-Jan	0520	2345	18:25	20	V	T
21-Jan	1230	1745	05:15	10	V	T
20-Jan	0830	1945	11:15	45	V	V
11-Jan	1250	2200	09:10	15	V	T
10-Jan	0945	2045	11:00	60	V	V
2-Jan	1330	1515	01:45	5	V	V
14-Dec	1600	0120	08:20	50	T	T
23-Nov	1100	1530	04:30	15	V	V
30-Oct	1800	2245	04:45	45	T	T
30-Oct	1200	1330	01:30	25	V	V
17-Oct	1820	2140	03:20	20	V	V
14-Oct	1630	2250	06:20	80	T	V

Rain rate and total event rainfall are derived from WSR-88D data using a Z-R relationship (Marshall and Palmer 1948). In so doing we quantify SCCZ precipitation over northern California regions lacking in situ measurements (Matrosov et al. 2014). Although numerous Z-R relationships exist, the "West Cool-Stratiform" relationship has been suggested for cool-season applications in the western US (Matrosov et al. 2014). The relationship is defined as:

$$Z = 75R^{2.0} \tag{4}$$

where Z is radar reflectivity in dBZ and R is rainfall rate in mm/hour. Quantitative precipitation estimates (QPE) were generated for the time period between convective initiation and dissipation for each event. Additionally, a total QPE of all 23 events was created in order to understand the contribution of these events to seasonal precipitation totals. Estimated event maximum precipitation of the most significant events ranged from 45-80 mm (Table 1), with long duration events most likely to have large rainfall totals.

b. Surface Observations

Surface observations in the NSV were obtained from the MesoWest cooperative network (Horel et al. 2002) in order to advance our understanding of surface flow characteristics contributing to SCCZ events. Stations used in this research include Chico Municipal Airport (KCIC), Red Bluff Municipal Airport (KRBL) and Redding Municipal Airport (KRDD) (locations shown in Fig. 1).

c. Operational Numerical Model Analyses

The National Centers for Environmental Prediction (NCEP) Rapid Refresh (RAP) model analysis data were used to examine atmospheric conditions over the study area

during SCCZ events. The RAP has 13 km horizontal grid spacing, 51 vertical sigma levels up to 10 hPa, and hourly time resolution (Benjamin et al. 2016). RAP analyses were obtained through the National Oceanic and Atmospheric Administration (NOAA) National Operational Model Archive and Distribution System (NOMADS). RAP data were used to produce composite analyses at surface through mid-tropospheric levels. The composites are centered on the time of SCCZ initiation, with T=0 specified as the initiation time for each event (listed in Table 1). All times were rounded to the nearest hour and composite maps were created for T-24 until T+24 to show the evolution of the synoptic conditions. For T-24 to T-6 and T+6 to T+24 composites were created every six hours, whereas between T-6 and T+6 composites were created every three hours in order to identify important transitions in background meteorological conditions that affect the SCCZ events. For each time, composite maps of surface, 850, 700, and 500 hPa level meteorological conditions were created.

In addition to map analyses, Skew-T/Log-P diagrams, wind profiles, and surface-based Convective Available Potential Energy (CAPE) and Convective Inhibition (CIN) time series were created for T-6 – T+6 interval. CAPE and CIN are important factors in convective storm development, including in orographic convection (Kirshbaum et al. 2018). Additionally, Kirshbaum and Durran (2005b) and Hagen et al. (2011) indicate that vertical wind profiles determine strength, structure, and location of orographic convective precipitation. Accordingly, hourly hodographs were produced for the 0-6 km layer to highlight shear characteristics during SCCZ events. Additional time series analyses are

also carried out by calculating values of N, Fr, and M, all of which have been shown to impact orographic precipitation (Houze et al. 2001; Hagen 2011; Kirshbaum et al. 2018).

d. Numerical Simulations

To gain a fuller understanding of the dynamics of the SCCZ than is possible from observations alone the Weather Research and Forecasting Model, version 3.8.1 (WRF) was used to simulate highly-organized SCCZ events on October 14th, February 8th and 9th, and March 21st and 22nd (See Table 1). These events represent the best examples of terrain (February 8th and March 21st) and valley (October 14th, February 9th, March 22nd) initiated convection, thus highlighting differences in the dynamics of these two types of events. These events were also among the longest and most organized of the 2016-17 season.

The WRF-ARW modeling system uses a non-hydrostatic, pressure-based, terrain following sigma coordinate (Skamarock et al. 2005). Simulations were run using two-way nesting across three domains containing 32 vertical levels up to 50 hPa. The outermost domain has a horizontal grid spacing of 12 km and is centered over the western United States with inner nests of 4km and 1.33 km centered over northern California (Fig. 2). Only output from the innermost 1.33 km domain is presented.

The simulations use the Thompson et al. (2008) microphysics scheme, Yonsei University planetary boundary layer (PBL) scheme (Hong et al. 2006), Rapid Radiative Transfer Model longwave radiation scheme (Iacono et al. 2008), Dudhia shortwave radiation scheme, the Noah land surface model for surface physics (Chen and Dudhia 2001) and the Kain-Fritsch 2 cumulus parameterization scheme (Kain 2004). The

cumulus parameterization schemes are only applied in the two outermost domains since the resolution of the innermost domain is considered to be “convective permitting”. Initial and boundary conditions were set using Global Forecast System (GFS) analysis data that updated every 6 hours through completion of each model run.

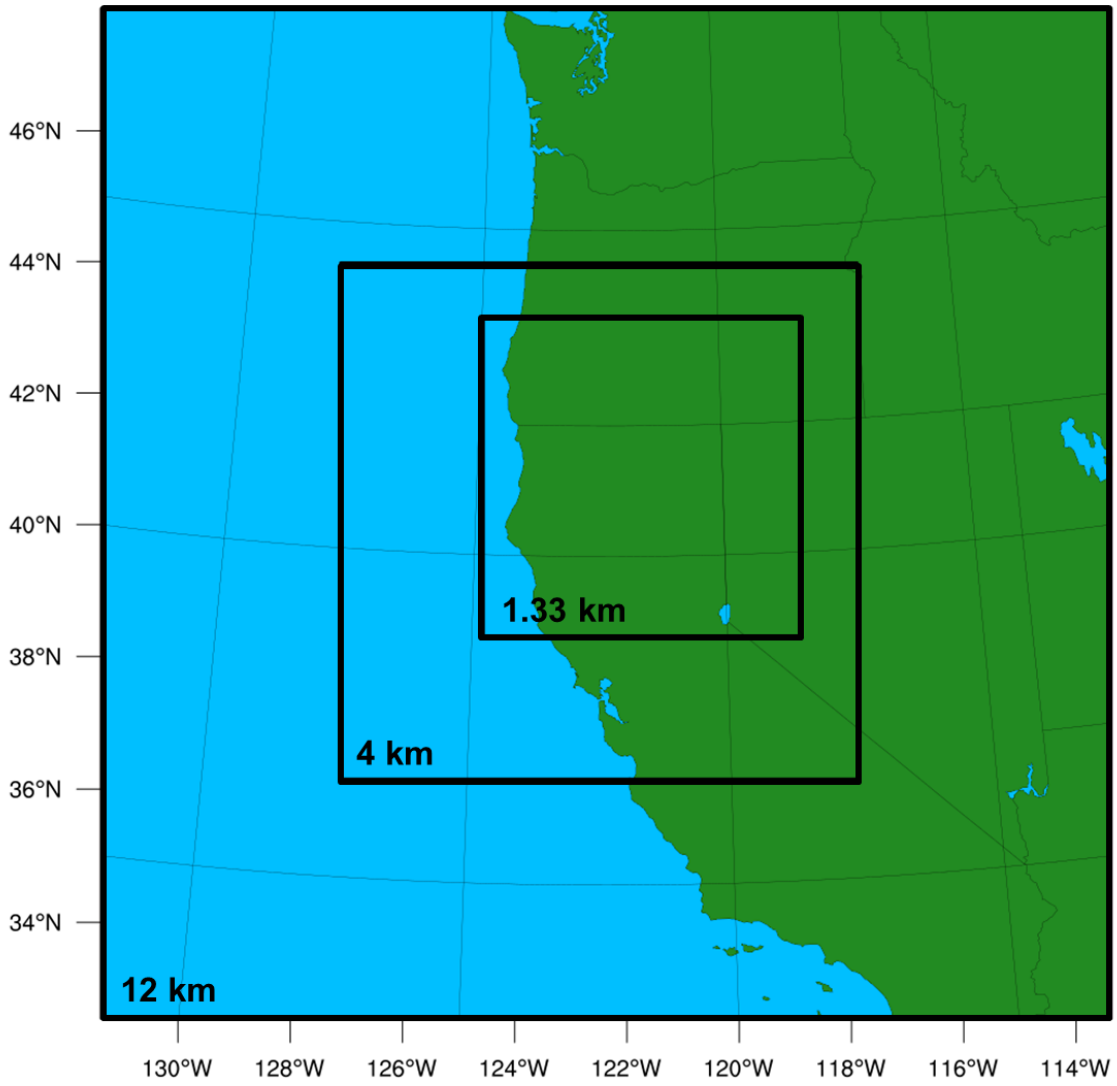

Fig. 2. WRF domain areas and respective grid spacing.

4. Results

4.1 Composite Analyses

SCCZ convective events typically occur during California's October-May wet season. The record setting 2016-17 wet season generated 23 SCCZ events, as summarized in Table 1. To understand the conditions necessary for event initiation, composites of the synoptic-scale mass, momentum and moisture fields were examined before, during, and after the convective initiation time of all events.

a. 500-hPa Composites

The composite 500-hPa geopotential height and momentum fields indicate that, like most California winter precipitation, SCCZ events are linked to a deep trough over the northeast Pacific Ocean and an associated eastward extension of the pacific jet into the west coast. To be specific, Figure 3 shows at T-24 there is a 500-hPa trough centered off the coast of Washington with west-southwesterly flow of 20-30 ms^{-1} over California and Oregon. The flow is weakly diffluent across much of the US west coast, and a jet maximum (>30 ms^{-1}) is located offshore of central California.

From T-12 through T-0 the trough deepens and moves east, allowing the jet maximum to approach, and then impinge on, the CA coast, generating a broad region of 25-30 m s^{-1} southwesterly flow across northern California. Of note, at T=0 the SCCZ is positioned under the left exit region of the 500-hPa jet, a region often linked to rising motion and dynamic destabilization, although the omega field indicates rising motion is only modest (2.5-5 Pa s^{-1}) and largely influenced by the topography. From T+6 through

T+24 the trough begins to fill and the jet weaken, though, interestingly the trough axis remains offshore, with no clear indication of a trough passage aloft.

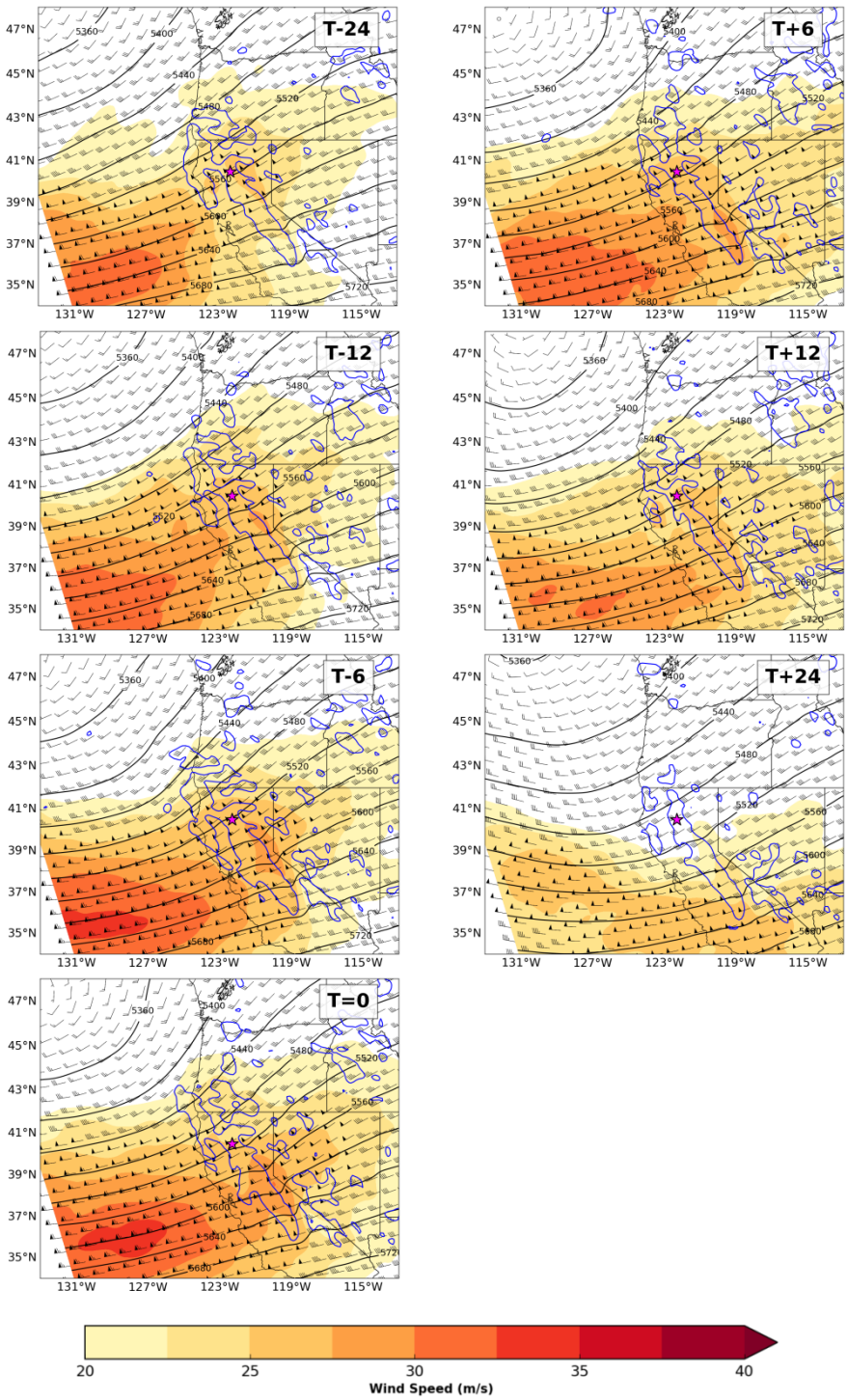

Fig. 3. 500-hPa geopotential heights (contours every 40m), winds (shaded, flag, full barb and half barb denote 25 ms^{-1}, 5 ms^{-1} and 2.5 ms^{-1}, respectively), and 700-hPa Omega (blue contour at -2.5 Pa s^{-1}) with the city of Redding indicated by a magenta star.

b. 700-hPa Composites

Figure 4 shows at 700-hPa relative humidity (*RH*) remains at or above 70% with southwest winds from 15-25 m s^{-1} through the duration of SCCZ events. The high *RH* in the mid-troposphere is an important factor for permitting deep convective clouds. In addition, since the 700 hPa surface is typically close to 3000 m MSL, and thus above all but the highest terrain (e.g., Mt. Shasta) in the vicinity of the SCCZ, the winds at this level serve as a reasonable diagnostic for the flow affecting the upper portion of the convective clouds associated with the SCCZ.

At T-24 cold air (-10°C) associated with the 700 hPa trough is situated over the northeast Pacific, with temperatures of -4°C and southwest winds of 15-17.5 ms^{-1} over the SCCZ. From T-12 to T=0, a broad region >80% *RH* expands to include the SCCZ and most of northern California. During this period, temperatures gradually decrease by about 1°C every 6 hours over the SCCZ (reaching <-6°C at T=0), with winds increasing to near 20 ms^{-1}. As we show later, the cooling at 700 hPa during this time decreases the stability of the lower troposphere.

From T+6 through T+24, the airmass over the NSV dries and the winds decelerate. For example, while the *RH* over the SCCZ remains in the 70-80% range from the T+6 through T+12 most of the surrounding air mass dries, and by T+24 drying overspreads much of the region. The end of the SCCZ window is also marked by a sharp reduction in 700 hPa winds.

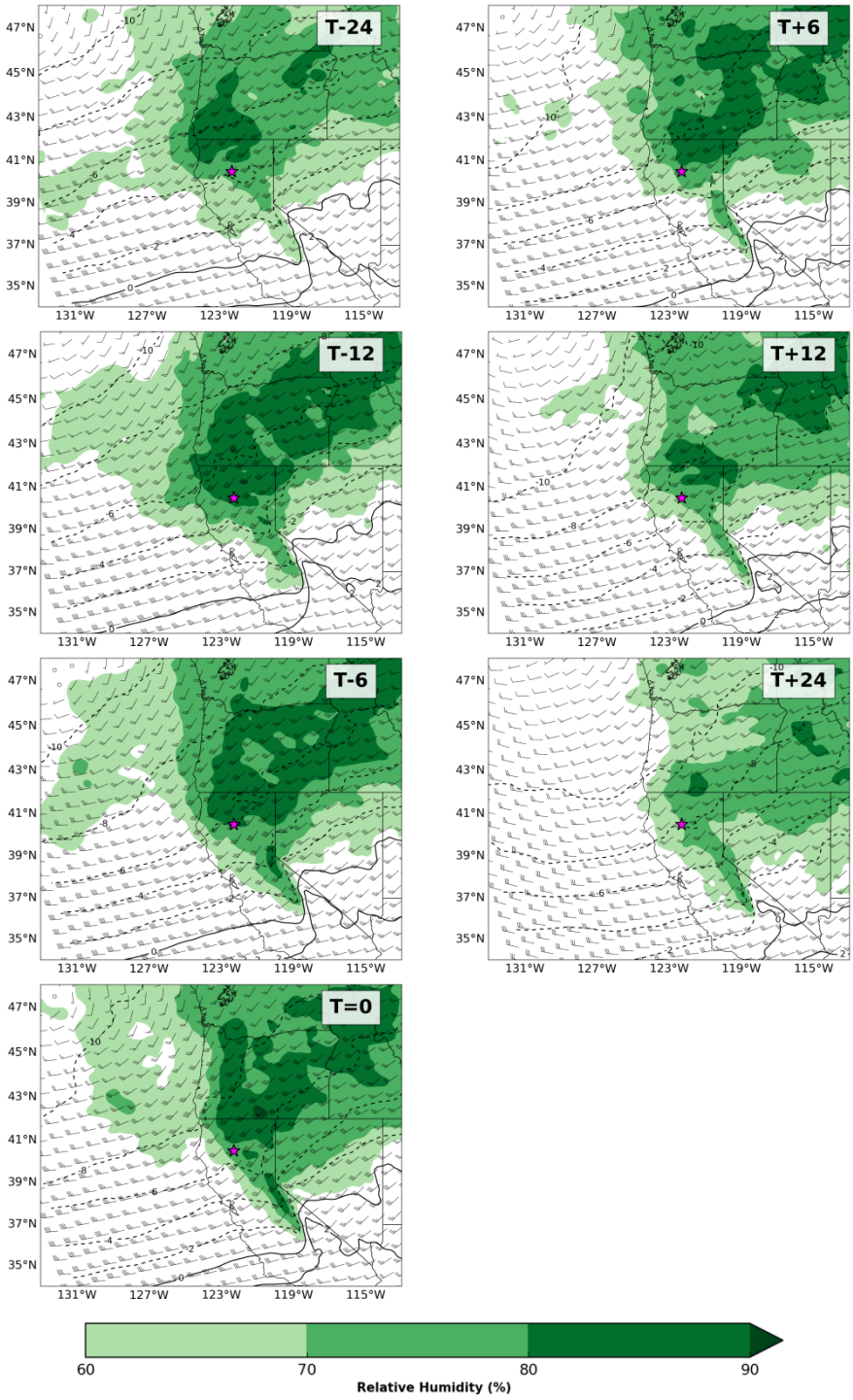

Fig. 4. 700-hPa temperature (contours every 2°C with negative contours dashed), winds (as in Fig. 3) and relative humidity (%, shaded), with the city of Redding indicated by a magenta star.

c. 850-hPaComposites

The 850 hPa composites represent flow near the crest of the topography (~1200 m) in the vicinity of the SCCZ. Figure 5 shows the development of barrier jets, apparent as maxima in the v-component of the wind, along both along the Oregon coast and the western slopes of the northern Sierra Nevada. The strongest 850 hPa height gradients and meridional wind maxima occur at T-12 and T=0 before weakening at T+6 and beyond. This composite is remarkably similar to that of the Sierra Barrier Jet (SBJ) (e.g., Neiman et al. 2010), which has been shown to impact precipitation rates and totals across the Trinity Alps, Trinity Mountains and northern Sierra due to changes in the SBJ.

The barrier jet in the NSV is associated with the along valley pressure gradient, which can be approximated using the difference in geopotential height between the San Francisco Bay Area (SFBA) to Redding. At T-24, there is 25 m difference in geopotential heights corresponding with south-southwest winds of 7.5-12.5 ms^{-1} over most of northern California, with the exception of the NSV where flow is southerly due to terrain channeling and the disruption of the geostrophic balance (i.e., down-gradient winds). By T=0, the SFBA to Redding height difference increases to ~30 m with a commensurate increase in 850-hPa meridional winds, which peak at ~15 ms^{-1} southeast of Redding. As we show later, these along valley winds are important in establishing the SCCZ. After T=0, both the height difference and winds diminish, with meridional flow dropping below 10 ms^{-1} during the cessation period (i.e., T+12 hrs).

Two additional notable features present at 850 hPa for the duration of SCCZ events: (1) a lee trough downstream of the northern California Coast Ranges and a commensurate

windward ridge along the western Sierra slopes, and (2) a region of consistently lower wind speeds west and north of Redding as compared to the strong meridional flow in the SBJ. Addressing the first point, the lee side trough and windward ridge are most evident from T-6 to T=0 when height gradients and meridional winds are also the most pronounced. Neiman et al. (2013) also identified blocking due to this windward Sierra ridge as a key component in maintaining meridional flow over the NSV. As the 850-hPa height gradient decreases and winds become more westerly, both trough and ridge weaken with the lee side trough shifting westward. As we show in the next section the lee trough is also apparent at the surface.

As indicated in the second point, there is a pronounced local minimum in wind speed both in the lee of the Coast Ranges west of Redding, and at the northern terminus of the NSV, north of Redding. There is therefore flow confluence (and convergence) of both the full wind and meridional-component of the wind in these regions, which is important for forcing the SCCZ convection. For example, there is a decrease in wind speed of 2-5 ms^{-1} between flow over the NSV and lower Trinity Mountains west of Redding, and a more substantial decrease of >5 ms^{-1} at the terminus of the NSV to the north.

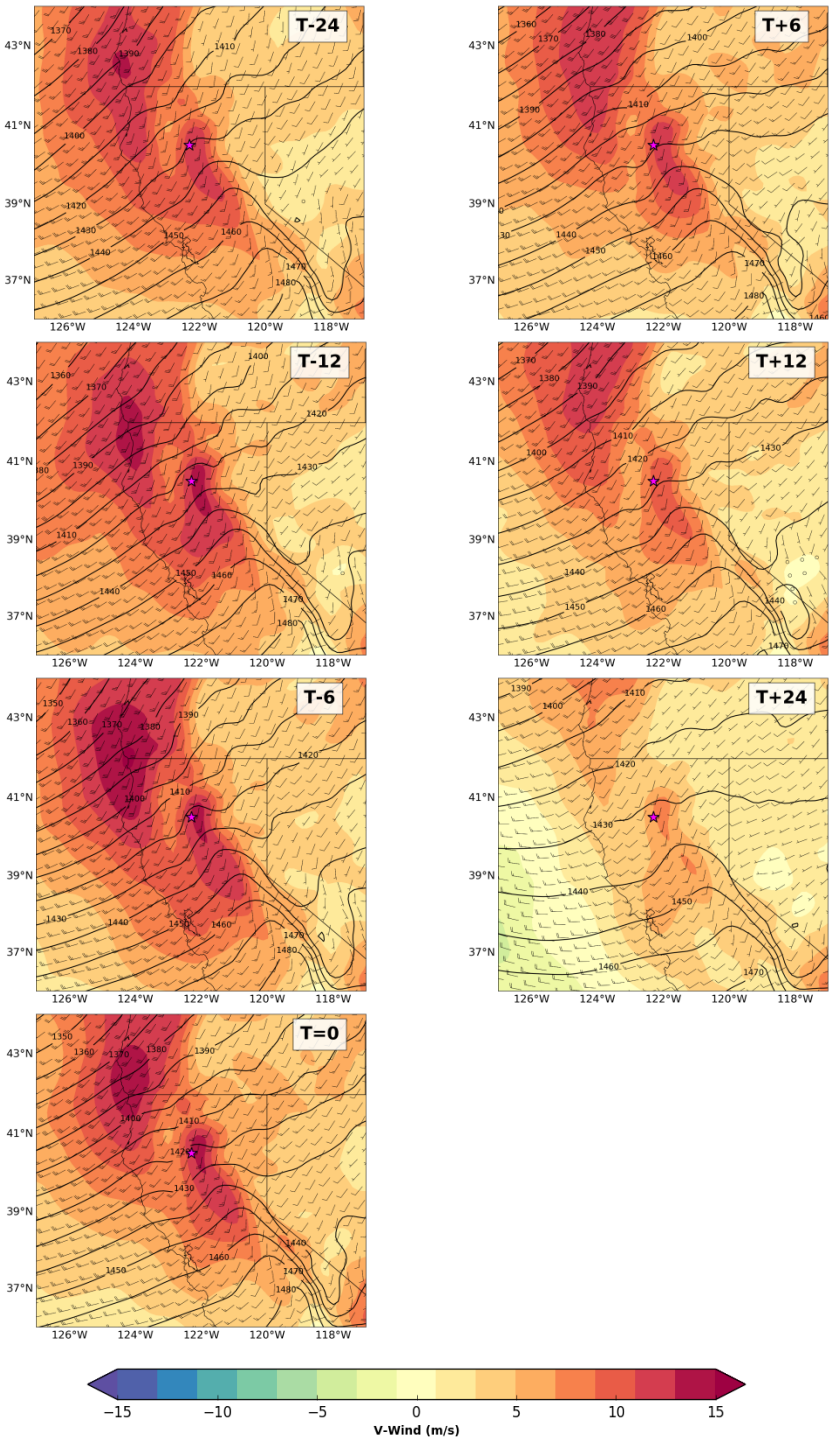

Fig. 5. 850-hPa geopotential heights (contours every 10m), winds (as in Fig. 3) and v-component wind (shaded), with the city of Redding indicated by a magenta star.

d. Surface Composites

The surface wind field, shown in Figure 6, shares many similarities with 850 hPa analysis in Figure 5, including the presence of the Sierra barrier jet and pronounced lee side trough over the NSV. However, unlike the upper level analyses (850-500 hPa), the surface winds in the NSV are nearly purely ageostrophic throughout the event, flowing down the gradient from higher to lower pressure (i.e. from south to north). The presumed mechanism for the ageostrophic flow is topographic pressure channeling (Whiteman and Doran 1993) and terrain blocking (Neiman et al. 2010). The ageostrophic flow up the NSV increases in concert with the increasing gradient in mean sea level pressure (MSLP) from T-24 to T=0 and then gradually weakens after T=0. To be specific, at T-24 the SFBA to Redding pressure difference is approximately 2.5 hPa, strengthening to ~4 hPa at T=0.

The minimum in MSLP at Redding at T=0 also corresponds to the peak amplitude of the leeside trough and a maximum in the v-component of the surface wind over the eastern portion of the NSV, which peak near 7.5 ms^{-1} to the south of Redding. Figure 7 shows significant confluence of the winds along the western NSV and both confluence and convergence at the northern terminus of the NSV at T=0, with a southwest to northeast oriented dilatation axis over and north of Redding (Fig. 7). The axis of dilatation indicate the direction and magnitude of "stretching" deformation, and is often linked to the organization of frontal features. Additionally, just south of Redding, the flow has a slight southeasterly component as a result of the surface trough deepening on the western edge of the NSV. This orientation favors flow perpendicular to the southeast

facing Trinity Mountains northwest of Redding (Fig. 1), which is apparent as strong convergence at the terminus of the NSV, north of Redding. The convergent region is collocated with both the observed location of the SCCZ on radar, and the SW to NE oriented dilatation axis in Figure 7.

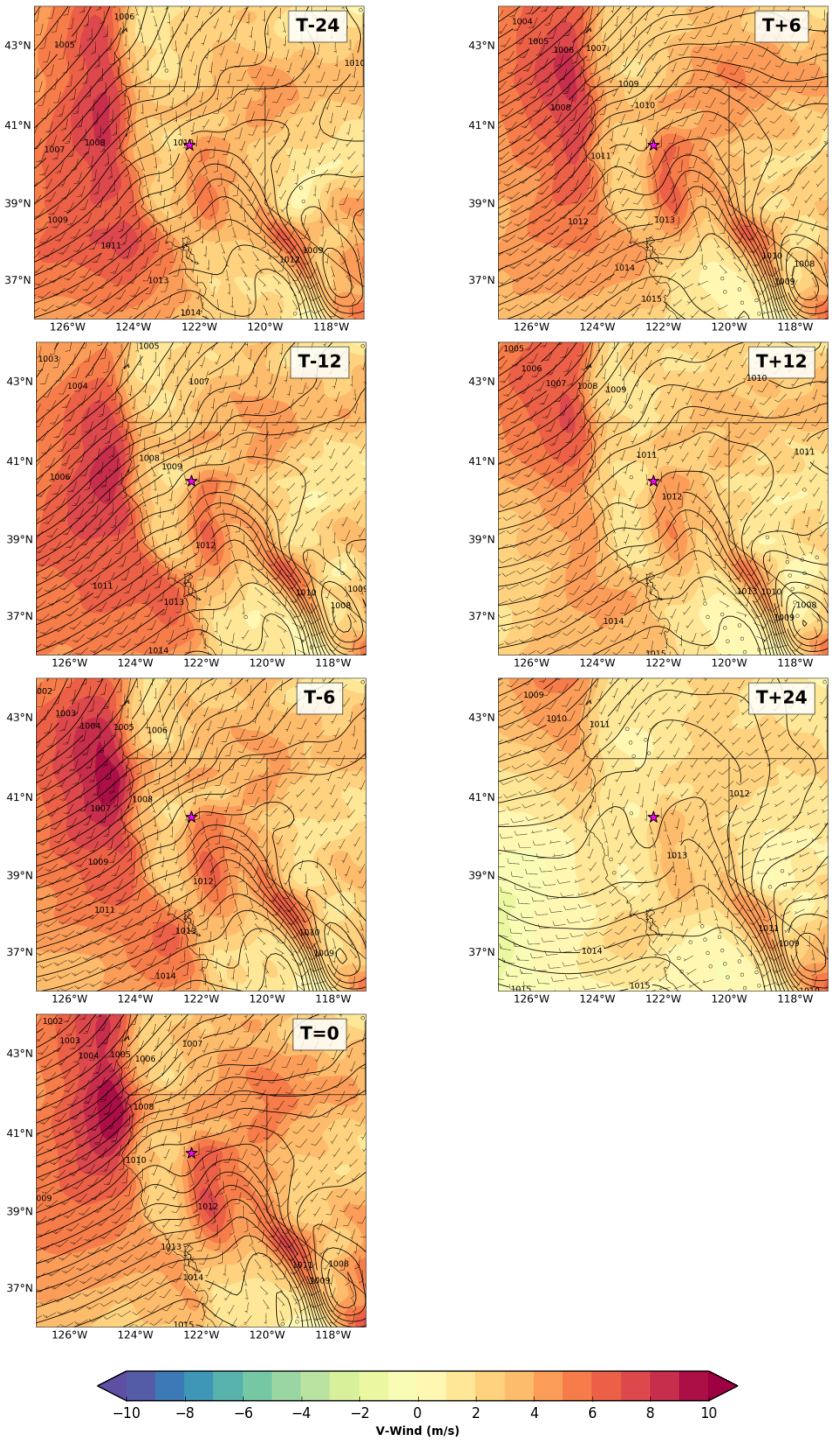

Fig. 6. MSLP (contours every 0.5 hPa), surface winds (as in Fig. 3) and v-component surface wind (shaded), with the city of Redding indicated by a magenta star.

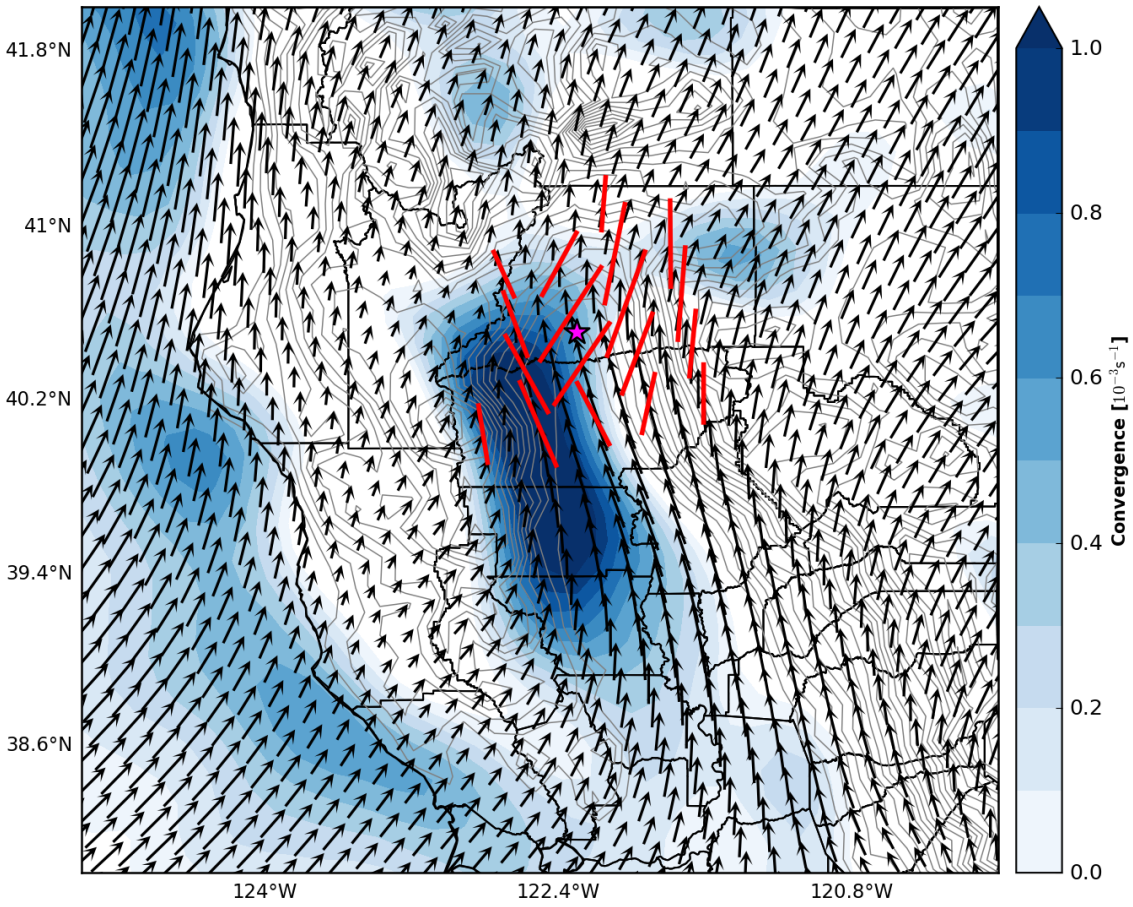

Fig. 7. Surface dilatation axes (red lines), wind (black vectors), convergence (shaded, s^{-1}), and terrain height (grey contours) with the city of Redding indicated by a magenta star.

e. Synopsis

Several synoptic features are common to the initiation of SCCZ convection, including:

1. A deep 500-hPa trough over the northeast Pacific along with a corresponding jet streak extending into central California.
2. High relative humidity (> 70%) at 700-hPa over northern California, with southwest winds >10 m s^{-1} above Redding.
3. Southerly, up-valley flow greater than 12.5 m s^{-1} at 850-hPa in the NSV corresponding to development of the SBJ
4. Development of a lee trough west of Redding combined with ageostrophic up-valley flow linked to a substantial MSLP differential between Redding and the southern Sacramento Valley.
5. Near surface axis-of dilatation oriented from SW-NE just north of Redding, CA

4.2 Case Analyses

Amongst the 23 SCCZ events in this study, we choose to conduct radar and thermodynamic analyzes of a subset of five long-lived events to elucidate some of the key physical processes impacting their evolution. The cases are (1) 14 October 2016, (2,3) 8 and 9 February 2017, and (4,5) 21 and 22 March 2017.

4.2.1 Radar Analyses

a. 14 October 2016

On 14 October 2016 SCCZ convection initiated following a cold front that moved through northern California around 1100 UTC (Fig. 8). Specifically, radar analyses show

an atmospheric river and associated cold front traverse Shasta County between 0700 and 1300 UTC, with scattered convection initiating in the post-frontal environment. By 2332 UTC an organized line of convection begins to develop over the SCCZ and persists until just before 0600 UTC on the 15 October (Fig. 9).

Figure 8 shows KBBX 0.5° radar reflectivity overlaid with surface wind observations at (a) 0800 and (b) 1100 UTC, prior to the SCCZ event. At 0800 UTC a broad region of light to moderate radar echoes (15-25 dBZ) covered the Trinity Alps and points west of Redding and Shasta Dam. Pre-frontal south-southeasterly flow was present across the NSV, with strongest winds of 7.5 m s^{-1} near Red Bluff and Redding. Light and variable winds of $\leq$2.5 m s^{-1} were present under the precipitation shield over the Trinity Alps. By 1100 UTC the cold front and associated atmospheric river had moved into Shasta County, evidenced by a narrow cold frontal rain band across south central Shasta County, a slight southwesterly wind shift in Redding behind the front, and an expansive area of moderate to heavy precipitation (30-45 dBZ) covering the majority of Shasta County. Southeast winds in the pre-frontal environment of the NSV range from 7.5-12.5 m s^{-1}, with post-frontal west-southwest winds around 7.5 m s^{-1} in Redding.

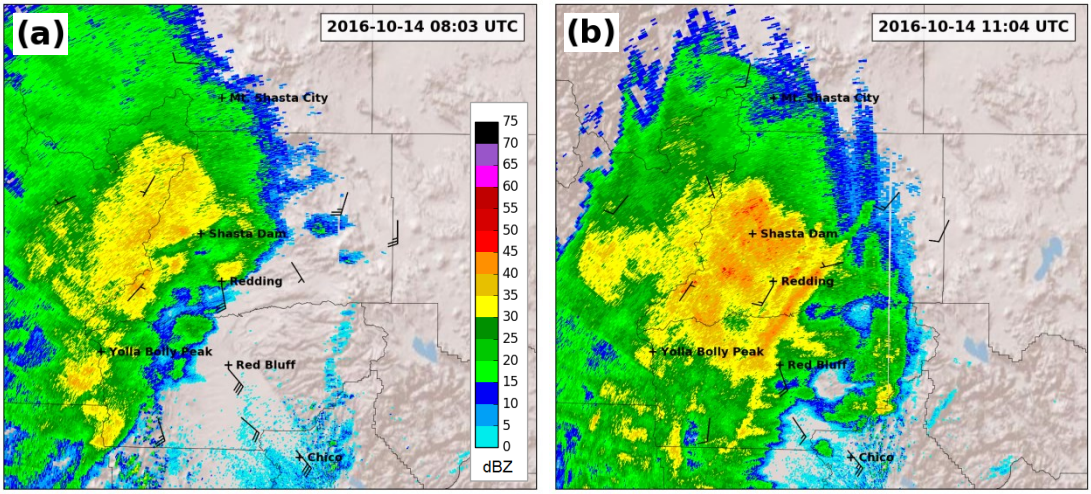

Fig. 8. KBBX 0.5° radar reflectivity [dBZ, shaded, scale in (a)] and MesoWest surface winds (full barb and half barb denote 5 ms^{-1} and 2.5 ms^{-1}, respectively) at (a) 0800 and (b) 1100 UTC 14 October 2016.

Figure 9 shows KBBX 0.5° radar reflectivity overlaid with surface wind observations at (a) 2300, (b) 0100, (c) 0200 and (d) 0400 UTC. At 2300 UTC disorganized, scattered convection had initiated north of Redding, with the strongest convective cells north of Shasta Dam (>40 dBZ). Compared to the prefrontal flow, the winds in the NSV have weakened (<7.5 m s^{-1}), but remain from the south-southeast despite the frontal passage (which is most evident aloft). Across the higher terrain east and west of Redding winds are west-southwesterly at 5-7.5 m s^{-1}.

By 0100 UTC (Fig. 9b) the initially scattered convection gives way to convection organized into a pronounced linear band between Shasta Dam and Redding with several radar echoes exceeding 50 dBZ. This is the onset of the SCCZ event (note actual start time is ~2332 UTC). The SCCZ convective line is oriented from southwest to northeast aligned with the topography northwest of Redding and directly in the lee (relative to the

SW flow aloft) of Yolla Bolly Peak to the southwest. Winds across the NSV remain 5-7.5 m s^{-1} except in Redding where winds have increased to 10 m s^{-1}.

By 0200 UTC (Fig. 9c) the SCCZ convection becomes more organized, back building to the southwest towards Yolla Bolly Peak while retaining its linear structure. The band axis rotated in a clockwise manner; moving the center of the band over Redding where winds dropped from 10 to 2.5 m s^{-1}. Elsewhere in the NSV, winds remain at 5-7.5 m s^{-1}, feeding low level air into the convergent convective line. The convective line remained quasi-stationary through 0300 UTC (not shown) before becoming transient and gradually diminishing in strength as it moved southward (Fig. 9d). By 0553 UTC no echoes exceeding 40 dBZ remained in the SCCZ or surrounding region. Based on these data we define the 14 October 2016 event as initiating at 2332 UTC and ending at 0553 UTC.

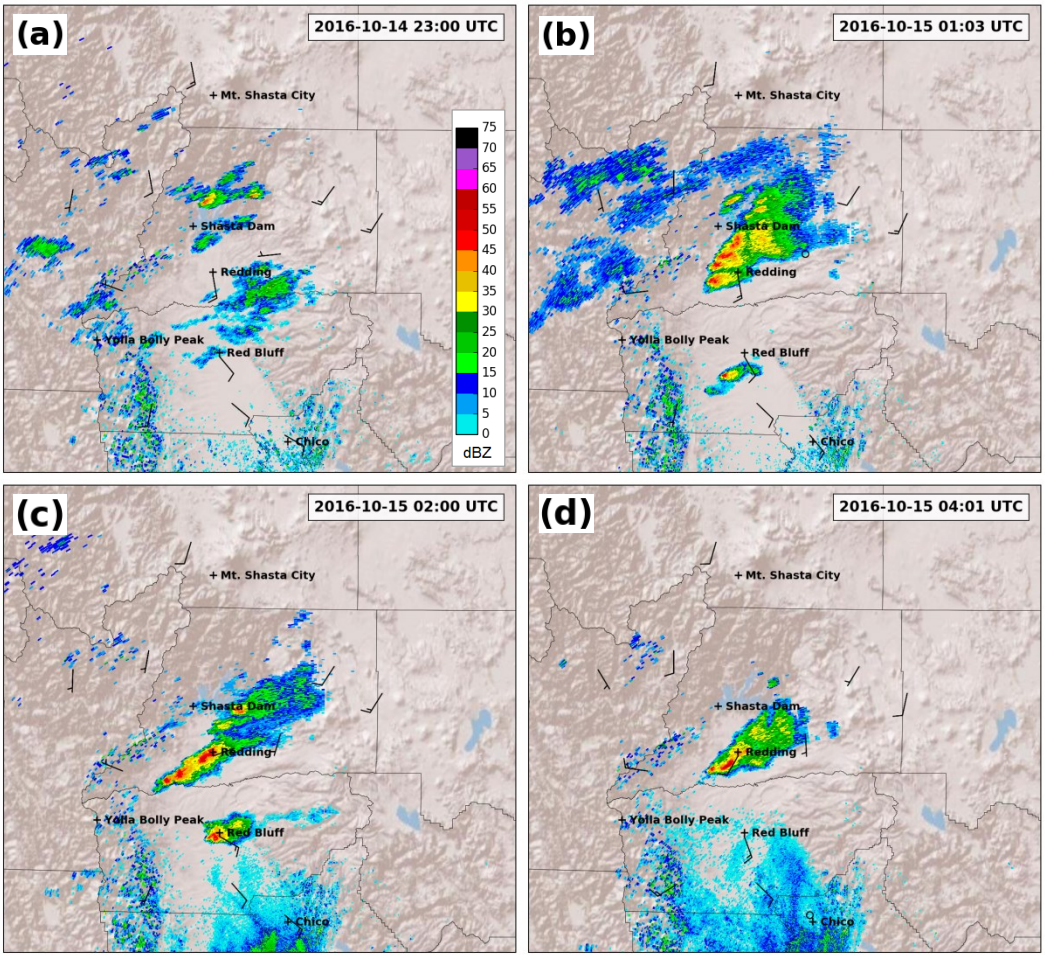

Fig. 9. KBBX 0.5° radar reflectivity (as in Fig. 8) and MesoWest surface winds (as in Fig. 8) at (a) 2300, (b) 0100, (c) 0200 and (d) 0400 UTC 14 and 15 October 2016.

The SCCZ evolution and impact is summarized using radar based quantitative precipitation estimates (QPE; i.e., cool season Z-R relationship, Eq. 4). The QPE shows localized and linearly organized accumulations of 5-35 mm between Redding and Shasta Dam during the seven hour event (Fig. 10). Within the broader region of accumulating rain, there are two distinct bands of enhanced accumulation. The northern band along the lower Trinity Mountains just south of Shasta Dam shows a narrow maximum of 30 mm of precipitation. This accumulation resulted from the initial burst of convection between

2330 UTC and 0030 UTC. Between 0030 UTC and 0100 UTC the convection moved southward, corresponding to a local maximum of ~80 mm resulting from the stationary and training nature of the convection through the remainder of the event. This event is notable in that the initiation is originally along the terrain, but then transitions to a long-lived high intensity linear convective feature over the valley.

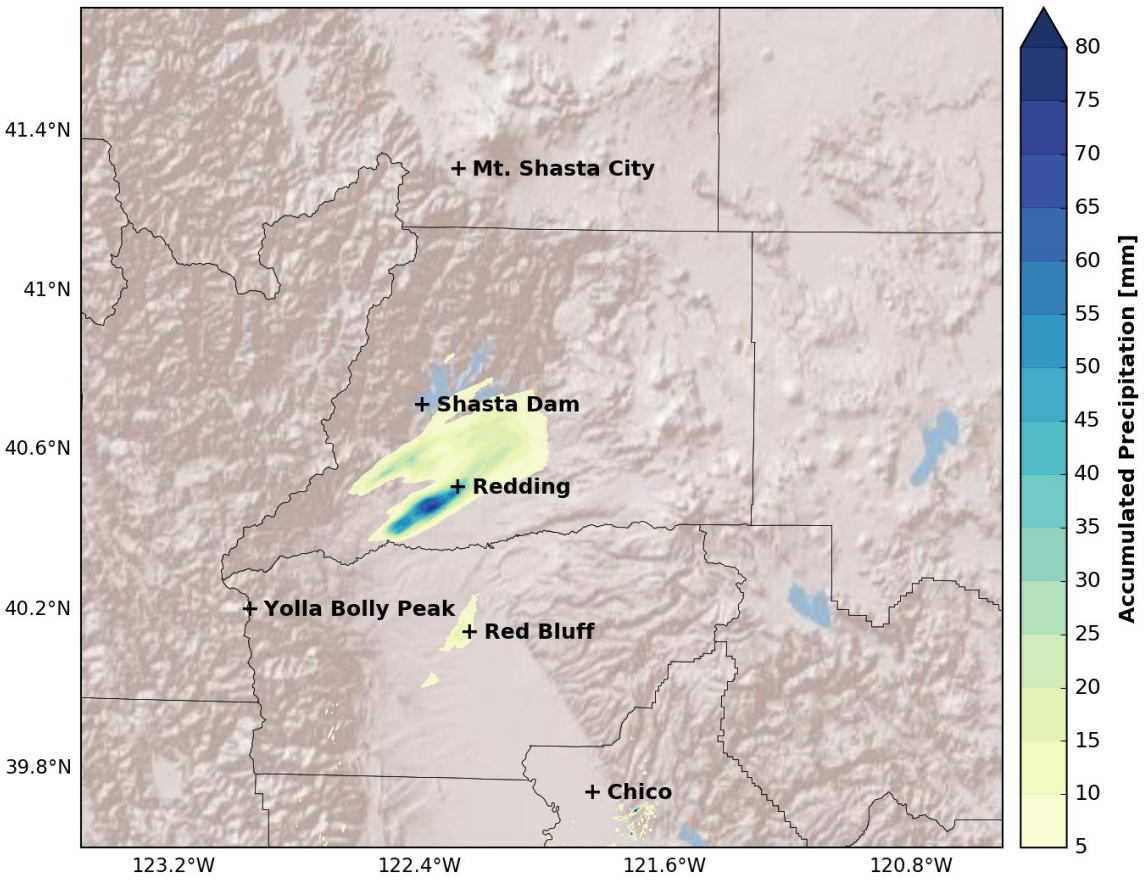

Fig. 10. KBBX quantitative precipitation estimate (shaded, mm, scale at right) from 2332 UTC 14 October 2016 to 0553 UTC 15 October 2016.

b. 8 February 2017

At 0000 UTC 9 February 2017 (1600 local time 8 February 2017) radar analysis show a SCCZ event initiated ahead of a frontal passage and, notably, embedded within a broader region of stratiform precipitation (Fig. 11).

The SCCZ convection was initially non-distinct due to a broad expanse of light to moderate radar echoes (15-30 dBZ) with localized bright-banding over western Shasta County (0000-0400 UTC, Fig. 11a). Then, starting around 0000 UTC, a southwest to northeast oriented band of 30-40 dBZ radar echoes emerged near Shasta Dam, and subsequently vacillated between just north and south of the dam (not shown). During this period the convection remained weak, with only a few echoes exceeding 40 dBZ. Winds across both the higher terrain and within NSV are of similar speed and direction (south southeast at ~10 m s^{-1}), indicating deep, prefrontal unidirectional flow over the region, suggesting that flow blocking is not at play in this event.

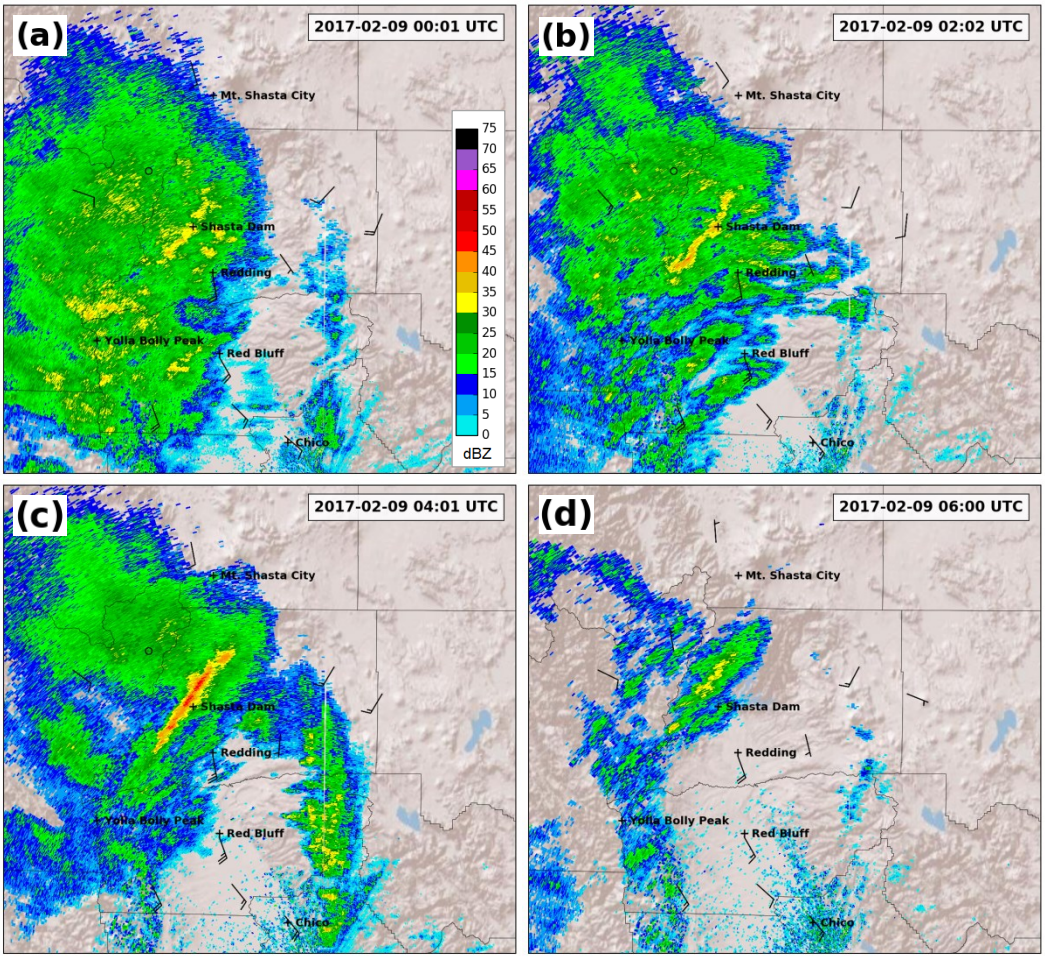

Fig. 11. KBBX 0.5° radar reflectivity (as in Fig. 8) and MesoWest surface winds (as in Fig. 8) at (a) 0000, (b) 0200, (c) 0400 and (d) 0600 UTC 9 February 2017.

By 0200 UTC the convective band becomes better organized with higher radar reflectivity (Fig. 11b). Specifically, a quasi-linear region of 40-45 dBZ radar echoes is positioned over Shasta Dam with an isolated 45-50 dBZ echo at the southwest end of the band (Fig. 11b). Notably, the band remains embedded within a larger region of stratiform precipitation. Winds in the NSV have increased slightly, with a maximum of 12.5 m s^{-1} in

Red Bluff. Elsewhere winds are relatively unchanged, with deep south-southeasterly flow of 7.5-10 m s^{-1} across the region.

By 0400 UTC SCCZ convection matured into a pronounced linear band of 40-45 dBZ radar echoes with embedded cells of 50-55 dBZ (Fig. 11c). The line is oriented from southwest to northeast along the upper Trinity Mountains just to the northwest of Shasta Dam. Radar animations at this time indicate that the band is almost stationary within the broader stratiform precipitation. The wind maximum in the NSV has expanded slightly as Red Bluff and Redding are both reporting 12.5 m s^{-1} south-southeast winds. Elsewhere, winds remain generally from the south at 5-10 m s^{-1}.

By 0600 UTC there is a marked decrease in the aerial extent of the stratiform precipitation and the SCCZ convection has weakened, shifting slightly northward. There remains a line of 30-35 dBZ radar echoes in the vicinity of the SCCZ just north of Shasta Dam (Fig. 11d). Winds have also weakened across the entire region, with 10 m s^{-1} winds in Redding and <10 m s^{-1} elsewhere. After 0600 UTC convection continues to transit out of the SCCZ as well as diminish in strength. By 0627 UTC only light and transient radar echoes remain near the SCCZ.

Using these radar data the 8 February 2017 event is defined as starting at 0000 UTC and ending at 0627 UTC 9 February 2017. The event QPE highlights the linear and localized nature of SCCZ convection and the significant enhancement of rainfall in the SCCZ as compared to the regions of stratiform rain (Fig. 12). To be specific, the widespread stratiform precipitation yields a broad area of 5-15 mm accumulations over eastern Trinity and western Shasta Counties. Embedded within this area is a localized,

linear region of 40-55 mm accumulations over the upper Trinity Mountains to the northwest of Shasta Dam. Notably, similar to the 14 October event the band axis appears to emanate from the immediate lee of Yolla Bolly Peak to the southwest.

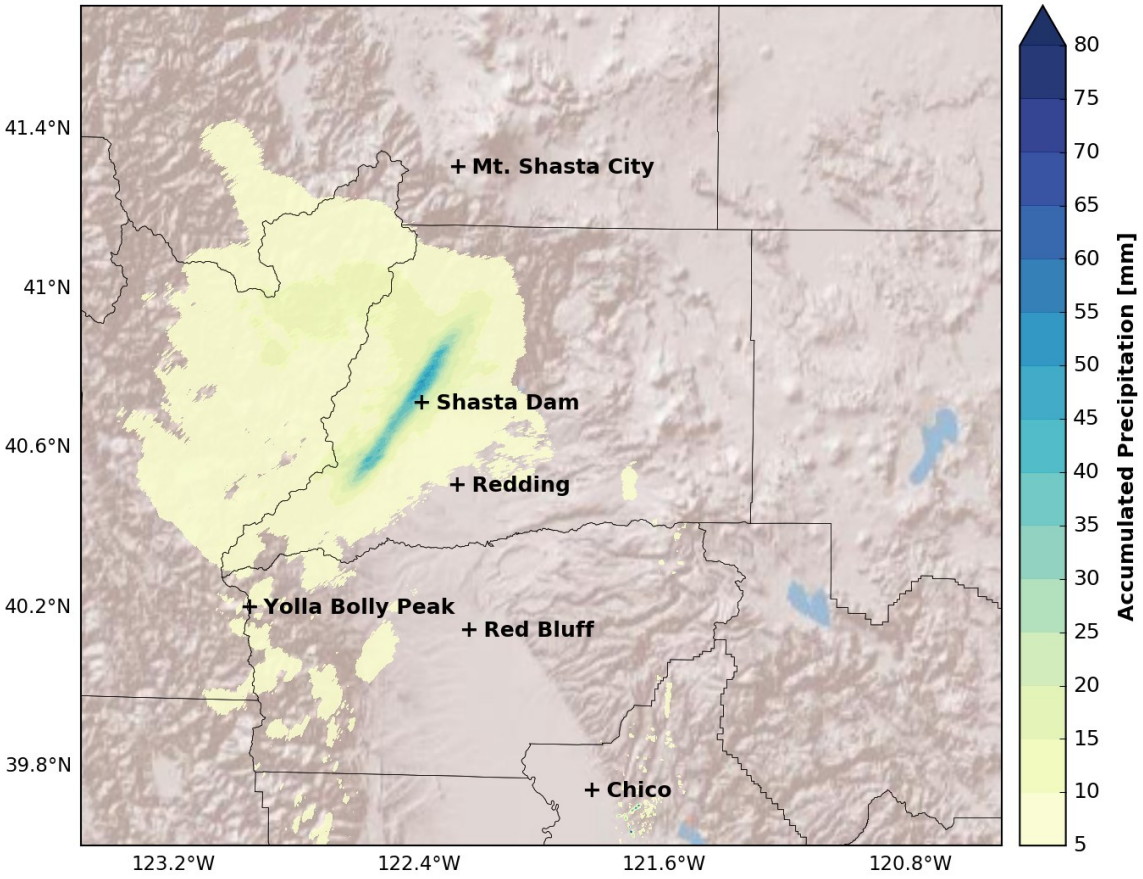

Fig. 12. KBBX quantitative precipitation estimate (shaded, mm, scale at right) from 0000 UTC to 0627 UTC 9 February 2017.

c. 9 February 2017

On 9 February 2017, the day after the previous event, SCCZ convection again initiated in the post frontal environment following an atmospheric river (AR) passage over northern California (Fig. 13). Unlike the previous event this SCCZ convection was

not embedded in a broader stratiform region of precipitation associated with the AR passage, which is apparent to the southeast of Redding in Fig. 13a.

At 2102 UTC 9 February 2017 a broad quasi-stationary band of 20-40 dBZ radar echoes was present over Shasta Dam and in the vicinity of the SCCZ (Fig. 13a). Stratiform rain associated with the antecedent AR is visible south of Red Bluff and near Chico (Fig. 13a). Notably, the winds across the higher topography of Shasta and Trinity Counties are generally southerly at 5-7.5 m s^{-1}, while within the NSV winds are stronger at 10-15 m s^{-1}, implying both convergent flow north of Redding and a low-level jet structure (i.e., strong winds close to the surface).

By 2300 UTC stratiform rain had exited the region and SCCZ convection had strengthened, with several 45-50 dBZ radar echoes embedded within a well-defined linear band of enhanced radar reflectivity (Fig. 13b). The core of the band was positioned just to the southeast of Shasta Dam over the lower Trinity Mountains. Winds in Redding remain about 15 m s^{-1}, however further to the south (e.g., Red Bluff) winds have weakened to 7.5-12.5 m s^{-1}.

The SCCZ continued to strengthen, and by 0100 UTC back-building extended the region of heavy precipitation to the southwest while the primary axis shifted south and east (Fig 13c). Multiple embedded cells at the southwest end of the band exceed 55 dBZ in strength, making this one of the stronger SCCZ events in the sample. Despite the change in position, winds remained at ~15 m s^{-1} in Redding with weaker winds to the south.

The southeastward progression and overall intensification of the SCCZ convection continued from 0100 and 0300 UTC, with the convective line situated slightly northwest of Redding by 0300 UTC (Fig. 13d). At that time the line consists of a nearly continuous band of 45-55 dBZ radar echoes and multiple waves are apparent. These waves are linked to mesovorticies that transited through the band (from southwest to northeast) between 0100 and 0200 UTC (not shown). By 0300 UTC winds have weakened region wide, generally $\leq$2.5 m s^{-1} in the mountains north of Shasta Dam and $\leq$10 m s^{-1} in Redding and points southward.

After 0300 UTC convection gradually dissipates from southwest to northeast along the band. By 0400 UTC the southwest terminus of the line is just north of Redding, with mainly 35-45 dBZ radar echoes remaining. After this time sporadic convection continues north of Redding for several more hours with occasional radar echoes exceeding 30 dBZ in strength. Due to the ambiguity regarding cessation of convection in the SCCZ, event termination was defined as the time at which the convective line lost its linear organization and heavy rainfall (<40 dBZ). Using these criteria the 9 February 2017 event initiated at 2029 UTC and terminated at 0447 UTC 10 February 2017.

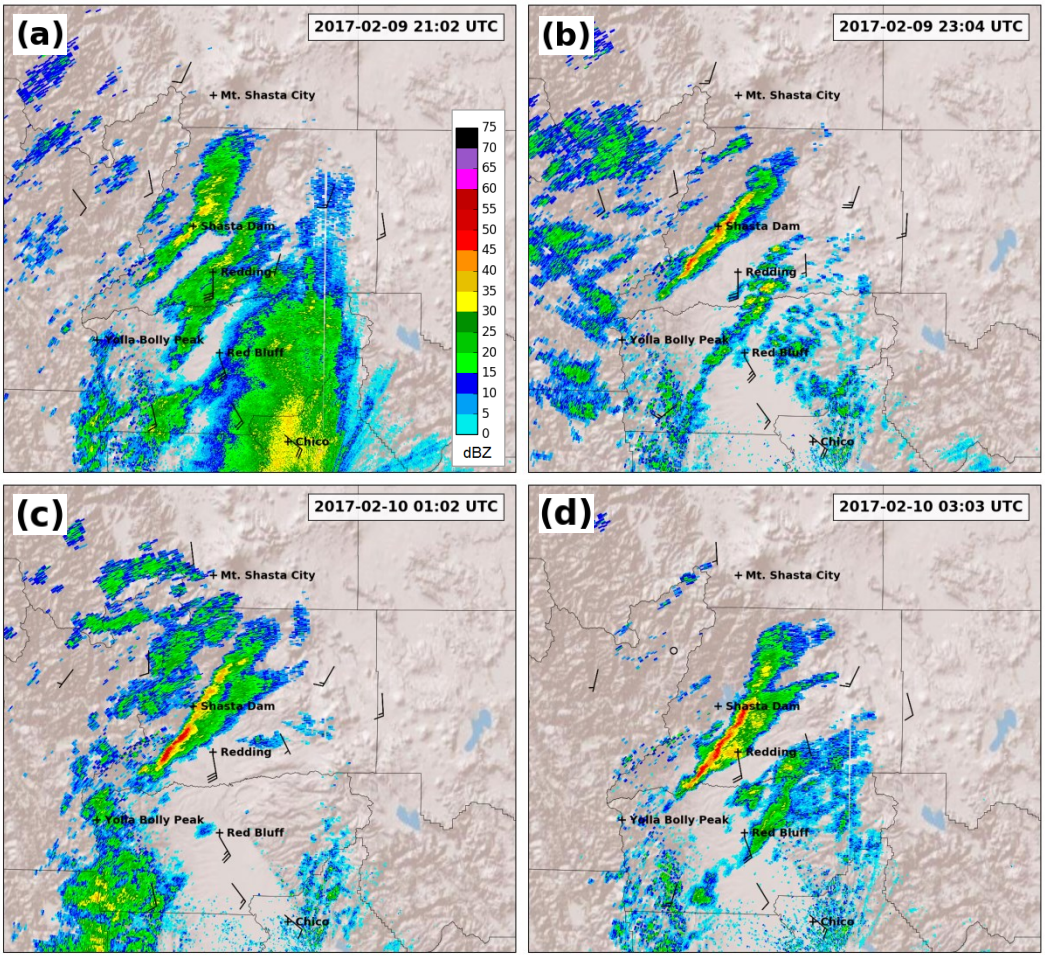

Fig. 13. KBBX 0.5° radar reflectivity (as in Fig. 8) and MesoWest surface winds (as in Fig. 8) at (a) 2100, (b) 2300, (c) 0100 and (d) 0300 UTC 9 and 10 February 2017.

QPE analysis from 2029 UTC to 0447 UTC highlights the slow southeast progression of the convection during the 9 February event (Fig. 14). The initial period of SCCZ convection resulted in accumulated rainfall of 30-50 mm in a narrow band over Shasta Dam. Localized amounts of 50-55 mm also occurred slightly southeast of Shasta Dam. The band then moved to the southeast, resulting in a broad area of 15-25 mm

accumulations between Shasta Dam and Redding. The QPE analyses also show a slight clockwise rotation in band orientation with time.

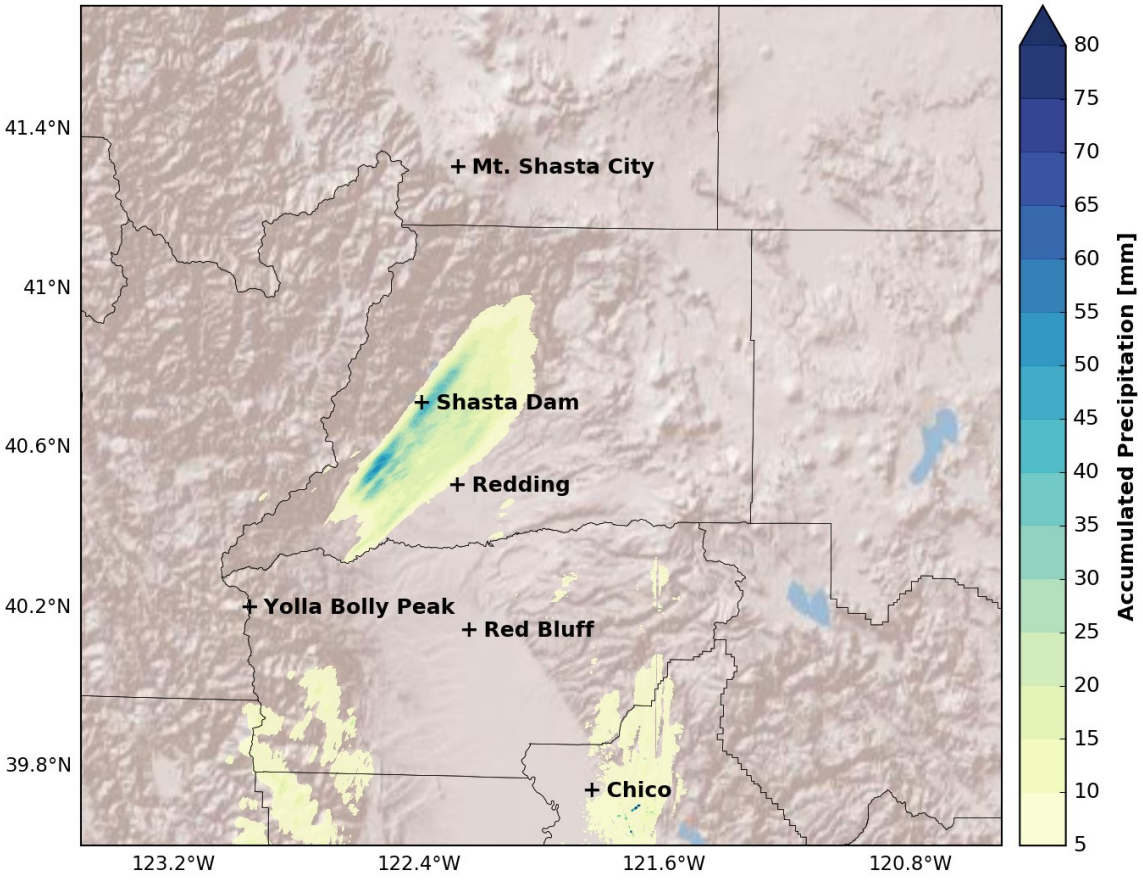

Fig. 14. KBBX quantitative precipitation estimate (shaded, mm, scale at right) from 2029 UTC 9 February 2017 to 0447 UTC 10 February 2017.

d. 21 March 2017

Around 1729 UTC on 21 March 2017 another SCCZ event initiated ahead of a land falling cold front. Figure 15a shows that convection was initially weak, with radar echoes of 30-40 dBZ in two adjacent and loosely organized convective lines north and east of Shasta Dam. Winds across the upper elevations of Shasta, Trinity and Tehama Counties are generally light ($\leq$5 m s^{-1}) and southerly. Winds in the NSV are southerly at 5-10 m s^{-1}.

Between 1830 and 1900 UTC the eastern line of convection dissipates and a band of 35-50 dBZ radar echoes strengthens north of Shasta Dam by 1900 UTC (Fig. 15b). Compared to previously analyzed SCCZ convection, this band has is more meridional as opposed to southwest-to-northeast in orientation. Additionally, a narrow band of light (20-30 dBZ) echoes is evident to the southwest of Shasta Dam as the line begins to back build along the topography. Winds across the Trinity and Shasta County mountains remain light and southerly, with winds of 7.5-10 m s^{-1} in the NSV. Winds in the Yolla Bollys of western Tehama County have shifted to the west-southwest and strengthened to around 7.5 m s^{-1}.

By 2000 UTC a well-developed south-southwest to north-northeast oriented line of 35-45 dBZ radar echoes extends across western Shasta County and over Shasta Dam, reflecting a mature SCCZ (Fig 15c). Winds remain 7.5-10 m s^{-1} out of the south in the NSV and weaker across the Trinity and Shasta County mountains. Westerly winds of ~10 m s^{-1} persist in the Yolla Bolly Mountains.

At 2100 UTC SCCZ convection has developed into a wide line of 40-50 dBZ radar echoes, though the southwestern terminus of the line has begun to move northward, likely

as a result of increased southerly flow within the NSV (Fig. 15d). Specifically, southerly flow has increased throughout the region, with Red Bluff and Redding reporting winds around 12.5 m s^{-1}. After 2100 UTC the convective band continues moving northward, with moderate (35-45 dBZ) reflectivities confined to regions north of Shasta Dam by 2200 UTC. Sporadic weak convection continues after 2200 UTC however by 2248 UTC radar echoes are no longer within the SCCZ and more transient showers are moving through the region.

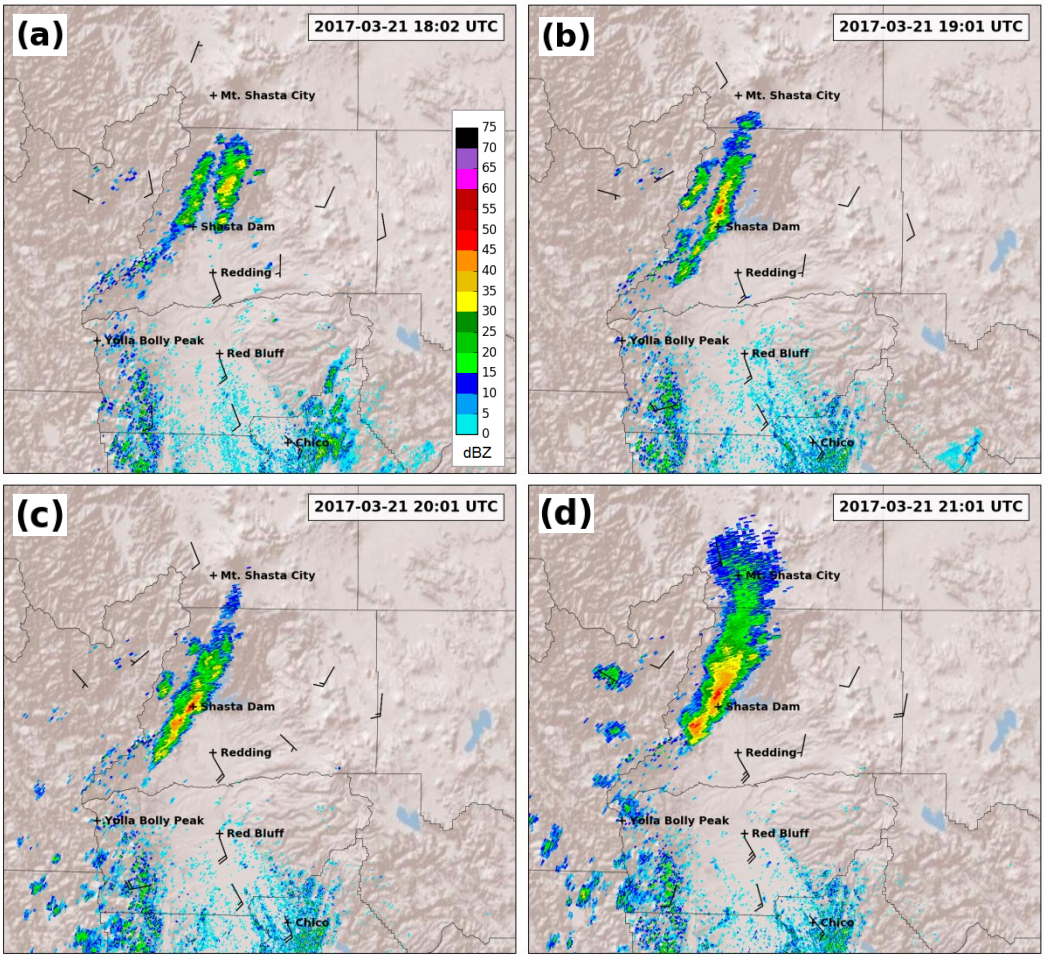

Fig. 15. KBBX 0.5° radar reflectivity (as in Fig. 8) and MesoWest surface winds (as in Fig. 8) at (a) 1800, (b) 1900, (c) 2000 and (d) 2100 UTC 21 March 2017.

Between 1729 UTC and 2248 UTC 21 March 2017 QPE analysis shows a narrow, linear band of enhanced accumulation just west of Shasta Dam (Fig. 16). The core of the rainfall accumulations are positioned over the watershed of Shasta Lake, where 30-35 mm of precipitation fell over the course of the event. Relatively persistent southerly flow during the event led to little deviation in convective line movement, resulting in the linear band of rainfall accumulations.

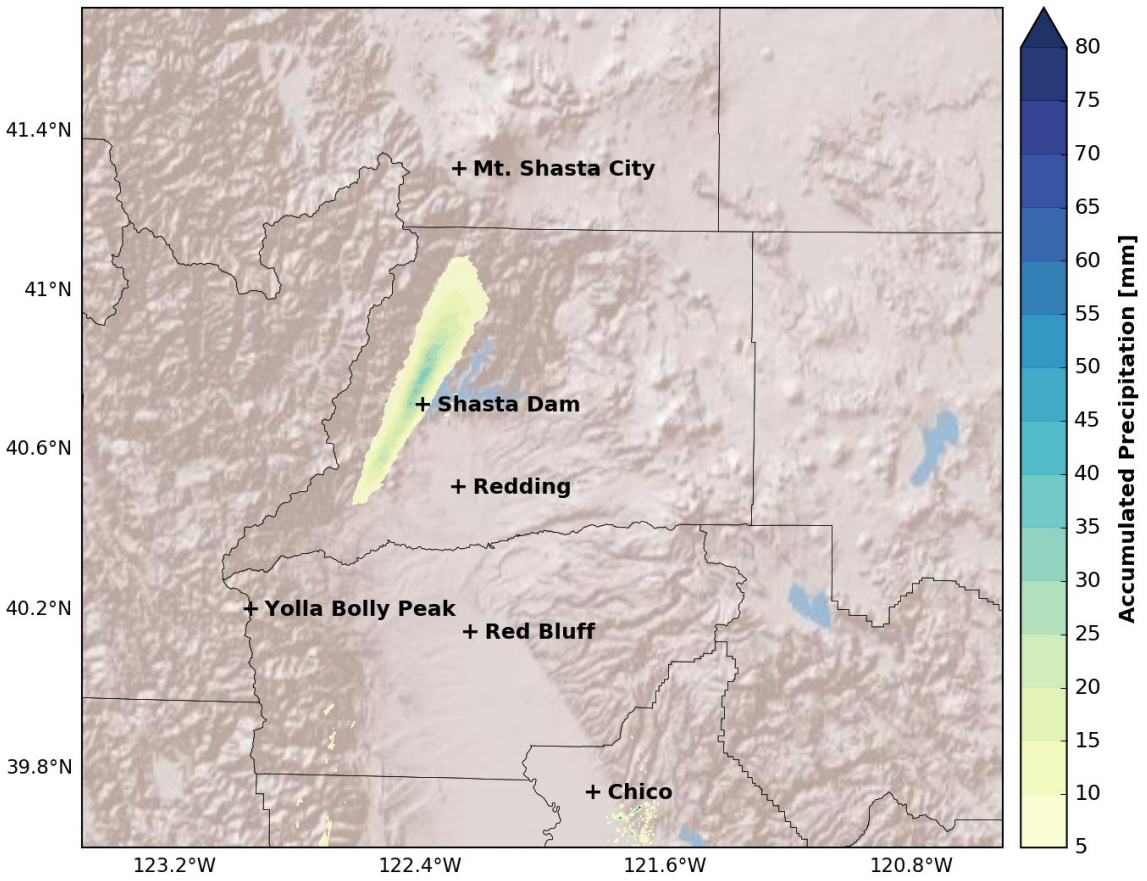

Fig. 16. KBBX quantitative precipitation estimate (shaded, mm, scale at right) from 1729 UTC to 2248 UTC 21 March 2017.

e. 22 March 2017

Following the qausi-stationary and generally meridional 21 March event, another more transient SCCZ event initiated near Redding the following day (22 March 2017). At ~1250 UTC convection initiated over the Trinity Mountains near Shasta Dam, as well as in the NSV southwest of Redding. Figure 17a shows the two parallel bands of moderate (30-40 dBZ) reflectivities in western Shasta and Northern Tehama Counties at 1300 UTC. The northern band is quasi-linear with higher reflectivities, while the southern band is more cellular. At this time winds are relatively light ($\leq$5 m s^{-1}) and variable outside of the NSV, while winds in the valley are south-southeasterly at 5-7.5 m s^{-1}.

By 1600 UTC the northern band of convection weakened considerably, while the southern band expanded in areal coverage and intensity (Fig. 17b). The southern band subsequently developed a linear region of 35-50 dBZ reflectivities stretching from northern Tehama County to northeast of Redding. New high reflectivity cells also initiated upstream of the band, back building the convective line to the southwest. While winds across the surrounding terrain remain unchanged; winds decreased by about 2.5 m s^{-1} throughout the NSV during this time. The weak NSV flow, compared to other cases, is notable as this case features the southernmost SCCZ position amongst our analyzed cases.

At 1900 UTC orientation of the line remains unchanged, but the core of high (40-50 dBZ) reflectivities has back built southwest into Tehama County (Fig. 17c). New cells continue to initiate along the topography of western Tehama County, training into the existing band. Winds in the NSV ahead of the band are southeast at 5-7.5 m s^{-1}, while

winds in Redding are variable at ≤2.5 m s^{-1} and likely under the influence of a precipitation induced cold pool.

As the convection continues to train over northern Tehama and southern Shasta Counties, cold pool dynamics begin to overwhelm other SCCZ influences. Specifically, by 2140 UTC the convectively generated cold pool induces an outflow boundary that pushes convection southward through the NSV and out of the region typically associated with the SCCZ (Fig. 17d). Over the next two hours this boundary pushes south through the entire NSV.

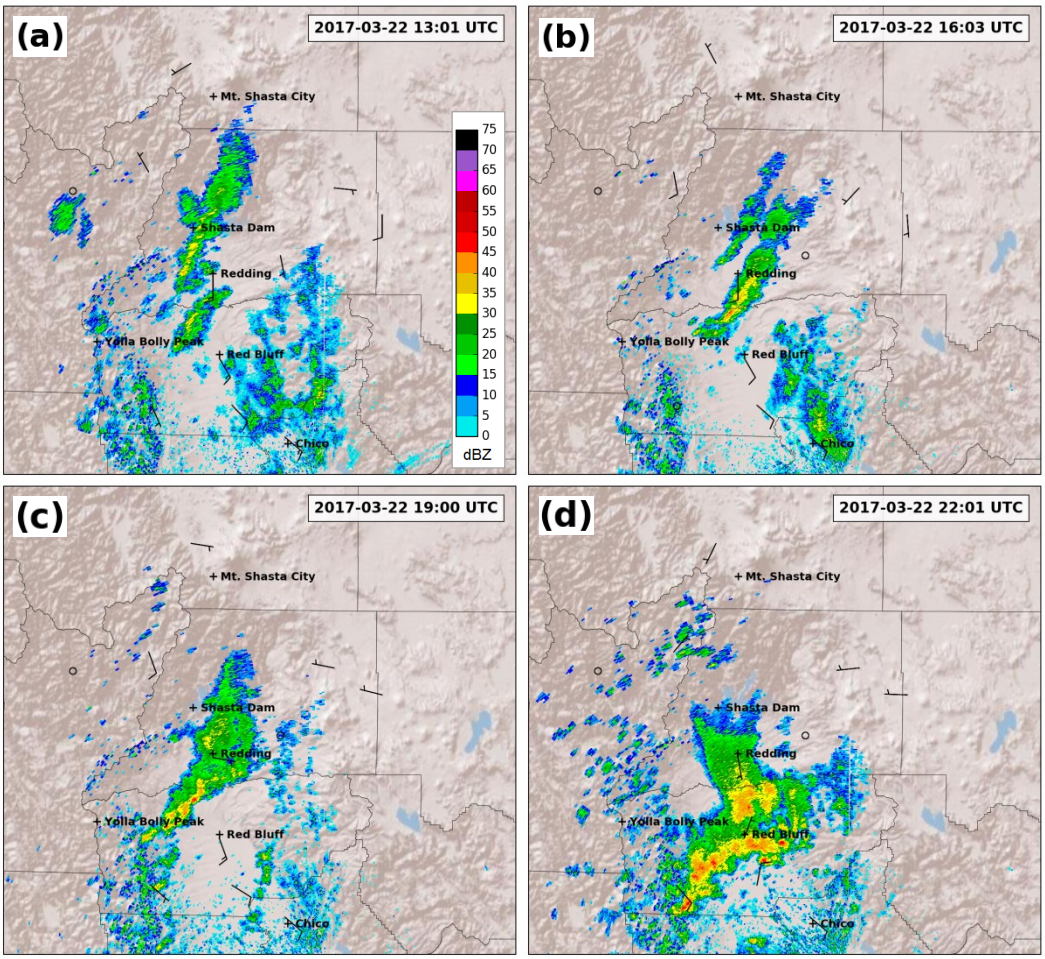

Fig. 17. KBBX 0.5° radar reflectivity (as in Fig. 8) and MesoWest surface winds (as in Fig. 8) at (a) 1300, (b) 1600, (c) 1900 and (d) 2200 UTC 22 March 2017.

QPE analysis shows the transient nature of this event compared to the SCCZ convection the previous day (Fig. 18). There is a broad area of 5-10 mm accumulations extending from central Shasta to central Tehama County, resulting from both the initial weak line of convection and southerly drift of the primary convective band. Within this area is a maximum along the county line of 40-45 mm of accumulation. Additional areas of heavy accumulations of up to 80 mm occurred in western Tehama County as a result of non SCCZ diurnal convection.

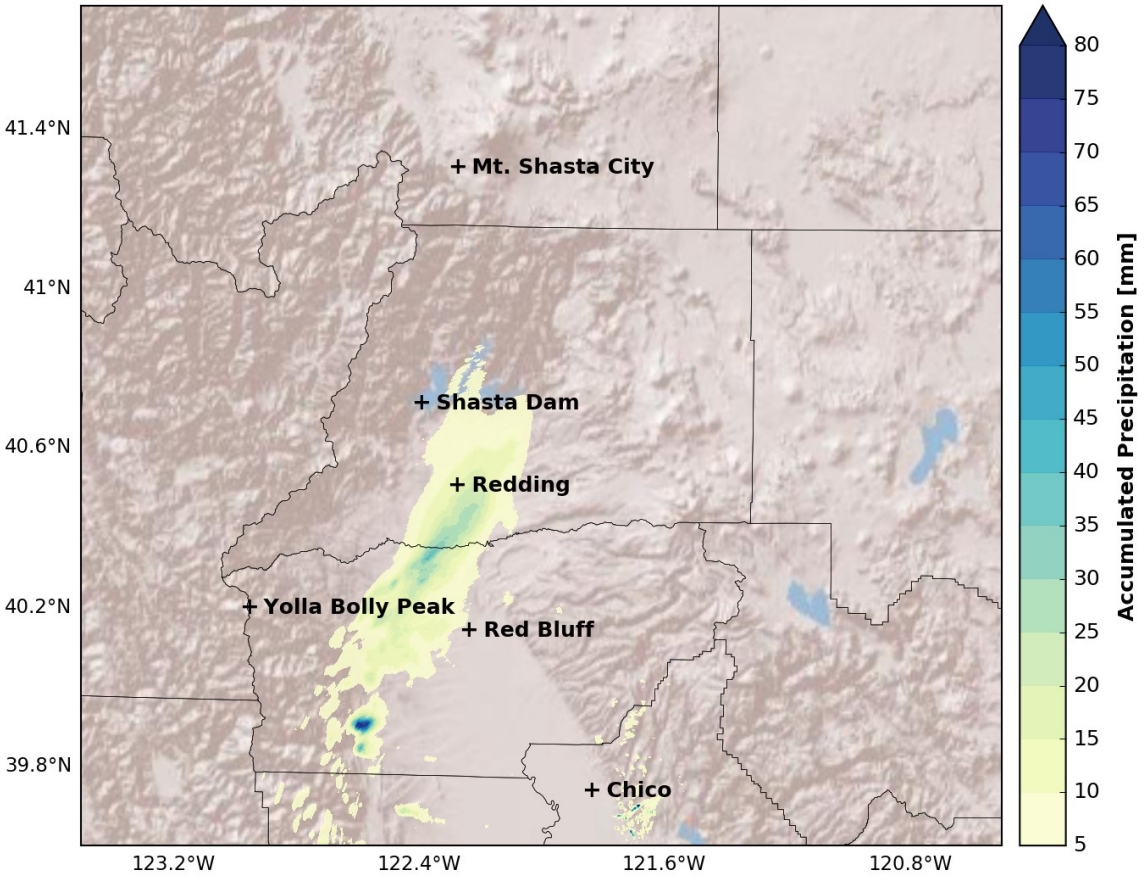

Fig. 18. KBBX quantitative precipitation estimate (shaded, mm, scale at right) from 1250 UTC to 2140 UTC 22 March 2017.

f. Precipitation Composite

In this section we examine the total contribution of SCCZ estimated rainfall to the 2016-2017 water year precipitation. Fig. 19a shows the California Nevada River Forecast Center (CNRFC) analysis of Oct 1 2016 – Sept 31 2017 (WY17) precipitation for the region. WY17 was a record setting season for many reporting stations throughout the regions, including a broad swath of precipitation totals exceeding 2500 mm (~100 inches) of liquid equivalent coincident with the SCCZ.

To estimate the SCCZ contribution to the overall seasonal total, we combine QPE for all 23 events (Fig. 19b). A semi continuous area of >100 mm covers most of southwest Shasta County including Shasta Dam and Redding and several embedded local maxima are apparent due to particularly high impact events. These maxima exceed 200 mm (7.87 inches) of seasonal precipitation in favored locations southwest of Redding and Shasta Dam. Although these maxima are quite localized, SCCZ precipitation contributes a notable percentage of seasonal precipitation region wide. Specifically, during 2016-17 SCCZ events contributed to broad areas of 5-10% seasonal precipitation in southwest Shasta County, with localized areas near 15% southwest of Redding, where the strongest events occurred. This analysis highlights the important role of SCCZ precipitation in contributing to local and regional water resources.

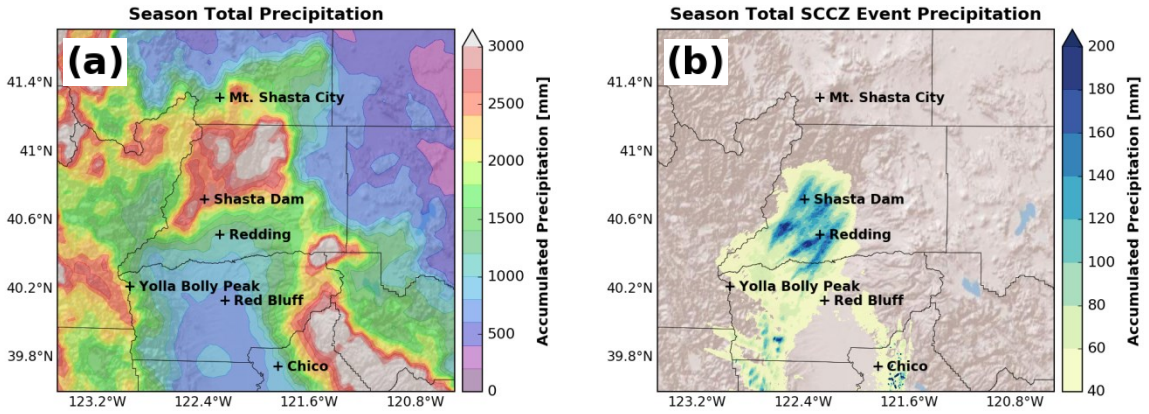

Fig. 19. (a) CNRFC WY17 total precipitation (shaded, mm, scale at right) and (b) KBBX QPE (shaded, mm, scale at right) composite of all SCCZ events October 2016 to April 2017.

4.2.2 Thermodynamic Analyses

For each of the previously discussed convergence events, thermodynamic, moisture and wind profiles were derived from hourly RAP analyses. Furthermore, convective (e.g., CAPE and CIN) and blocking (e.g., non-dimensional mountain height [M]) parameters were calculated from the RAP analyses to examine environmental conditions surrounding SCCZ convection.

a. 14 October 2016

Figures 20a and 20b indicate the 14 October event was associated with potential instability in the lower troposphere (i.e., the pronounced layer of dry air between 800 and 500-hPa capping a warm, moist boundary layer) coupled with modest wind shear, as indicated by the sharply curved hodograph below 1km, and straight-line hodograph from 1-6 km during convective initiation (Fig. 20b). This thermodynamic state is remarkably similar to that associated with orographically forced linear convective features

documented in Kirshbaum and Durran (2005b). Additionally, a moist-adiabatic profile in the upper troposphere, veering winds, and an increasingly curved hodograph over time support the organization of deep convection during the SCCZ event. While modest conditional instability (i.e. 350-400 J kg^{-1} of CAPE at 2200 UTC in Fig. 20c) may influence convective initiation, the strongest radar reflectivities during the SCCZ event occurred between 0200 and 0400 UTC during a period of zero surface-based CAPE and substantive (-40 J kg^{-1}) CIN. The CIN, low CAPE and gradually decreasing surface temperatures indicate surface-based thermal processes are not a primary mechanism of SCCZ convection.

Rather, the convection appears to be triggered by mechanical lifting of the meridional up valley flow as it impinges on the northeastern Trinity Mountains. The resulting forced convection is subsequently organized into a linear feature by the lower tropospheric wind shear. Specifically, near surface winds of 5-10 m s^{-1} veer with height, becoming southwest, west-southwest, and then west at 10, 20, and 40 m s^{-1}, respectively. At convective initiation (dashed black line) the hodograph is approximately a straight line, which Kirshbaum and Durran (2005b) show to be a key component of linearly organized orographic convection. As time progresses the hodograph becomes more curved, with southerly flow increasing to 10-15 m s^{-1} in the lowest 1 km and flow becoming more westerly at 5-6 km. This transition corresponds with the line developing more cellular characteristics and stationary back building seen southwest of Redding.

The flow blocking parameter (M, shown in Figure 20d) shows the southerly flow highly susceptible to blocking until about 0200 UTC, after which flow varies from

unblocked to weakly blocked. Houze et al. (2001) and Grossman and Durran (1984) suggests such unblocked flow should support more widespread precipitation over the terrain where the air mass is lifted. During this unblocked period convection moved southward over Redding, suggesting convection was initiated by the shallow moist layer below 900-hPa (Fig. 20a) being lifted over the low hills of the NSV. Strength and movement of the convection was likely influenced by other mechanisms like wind shear, and potentially near surface cold pool dynamics that are not well resolved in observations or model analysis fields.

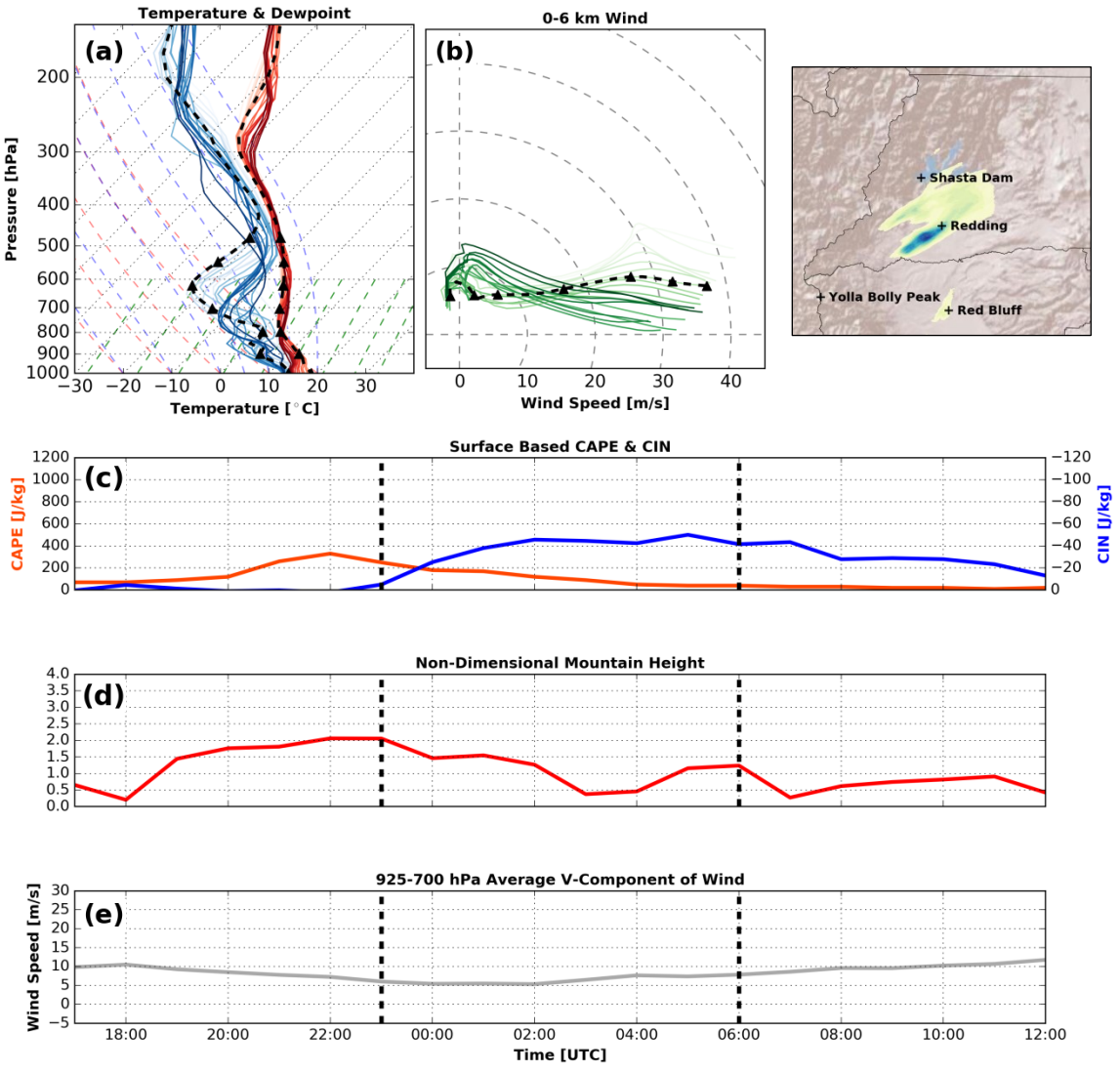

Fig. 20. RAP derived vertical profiles over Red Bluff of (a) temperature (°C, red) and dew point (°C, blue) and (b) winds from 0 to 6 km (m s^{-1}, green). Shading represents forward progression in time from light to dark, with convective initiation shown by a black dashed line. Black triangles indicate 1 km intervals starting at 0 km and ending at 6 km. RAP derived time series of (c) CAPE (J kg^{-1}, orange) and CIN (J kg^{-1}, blue), (d) non-dimensional mountain height (red) and (e) 925-700 hPa layer average meridional wind (m s^{-1}, grey). All parameters starting 6 hours prior to convective initiation (1700 UTC 14 October 2016) and ending 6 hours after cessation (1200 UTC 15 October 2016). Initiation and cessation times are indicated by black dashed lines in (c), (d) and (e). Event total precipitation in upper-right for reference.

b. 8 February 2017

Radar analyses (Fig. 11a-c) revealed that the 8 February SCCZ event was morphologically distinct from others, in that the linear convective feature was embedded within a broader region of stratiform precipitation. Figure 21 elucidates some of the distinguishing dynamical factors, as well as some similarities, between the 8 February and 14 October events. The similarities include a moist adiabatic upper troposphere (Fig. 21a) and a gradual transition to a straightening (i.e, more linear) hodograph over the course of the event (Fig. 21b). A key difference, however, is the absence of substantive potential instability (Fig. 21a,c). Rather the profile is close to moist adiabatic (i.e., neutrally stratified with respect to saturated parcels) through the depth of the troposphere and for the duration of the event; consistent with the presence of widespread stratiform precipitation (Fig. 11a-11c). As expected with a nearly saturated profile, very little CAPE (<200 J kg^{-1}) and CIN ($-20\leq$ J kg^{-1}) are present, again suggesting that mechanical lifting is necessary to initiate and sustain deep convection (Fig 21c). A shallow (800-600 hPa) dry layer develops towards the end of the event, coinciding with the dissipation of stratiform precipitation (Fig. 11d).

In addition to differences in the convective potential, the layer-averaged meridional flow is significantly stronger on 8 February than 14 October. Up valley flow (i.e., a south wind) increases from ~10 to 20 m s^{-1} in the period leading up to convective initiation at 0300 UTC, whereas during the Oct 14 event the flow remained weaker than 10 m s^{-1}. Throughout the remainder of the Feb 8th event winds remained near 20 m s^{-1}. The high flow speed and nearly moist-neutral stratification result in persistent unblocked flow

(M~0.5; Fig. 21d), which also differs from the Oct 14 case which featured some blocking characteristics and a wider range of conditions (i.e, M ranging from 0.5 to 2). The consistent positive meridional winds and unblocked conditions favor orographic precipitation enhancement over the Trinity Alps and Trinity Mountains rather than over the upstream valley locations.

When this saturated upslope flow is combined with the wind shear depicted in Figure 21b, linear convection becomes possible. As noted by Kirshbaum and Durran (2005b), convection initiated due to topographic roughness can be organized into stationary linear bands under conditions with unidirectional wind shear. At the onset of SCCZ convection the hodograph is curved, with southerly surface flow of ~10 m s^{-1} veering to west-southwest at ~25 m s^{-1} at 3km and above. As the event progresses, surface winds remain consistently from the south while upper level winds become more southwesterly and increase to nearly 40 m s^{-1}. We hypothesize that the increasing flow aloft shears apart newly developing cells after 0600 UTC, apparent in the radar reflectivity as reduced convective coverage and intensity as well as a rapid northward advection of remaining radar echoes (Fig. 11d).

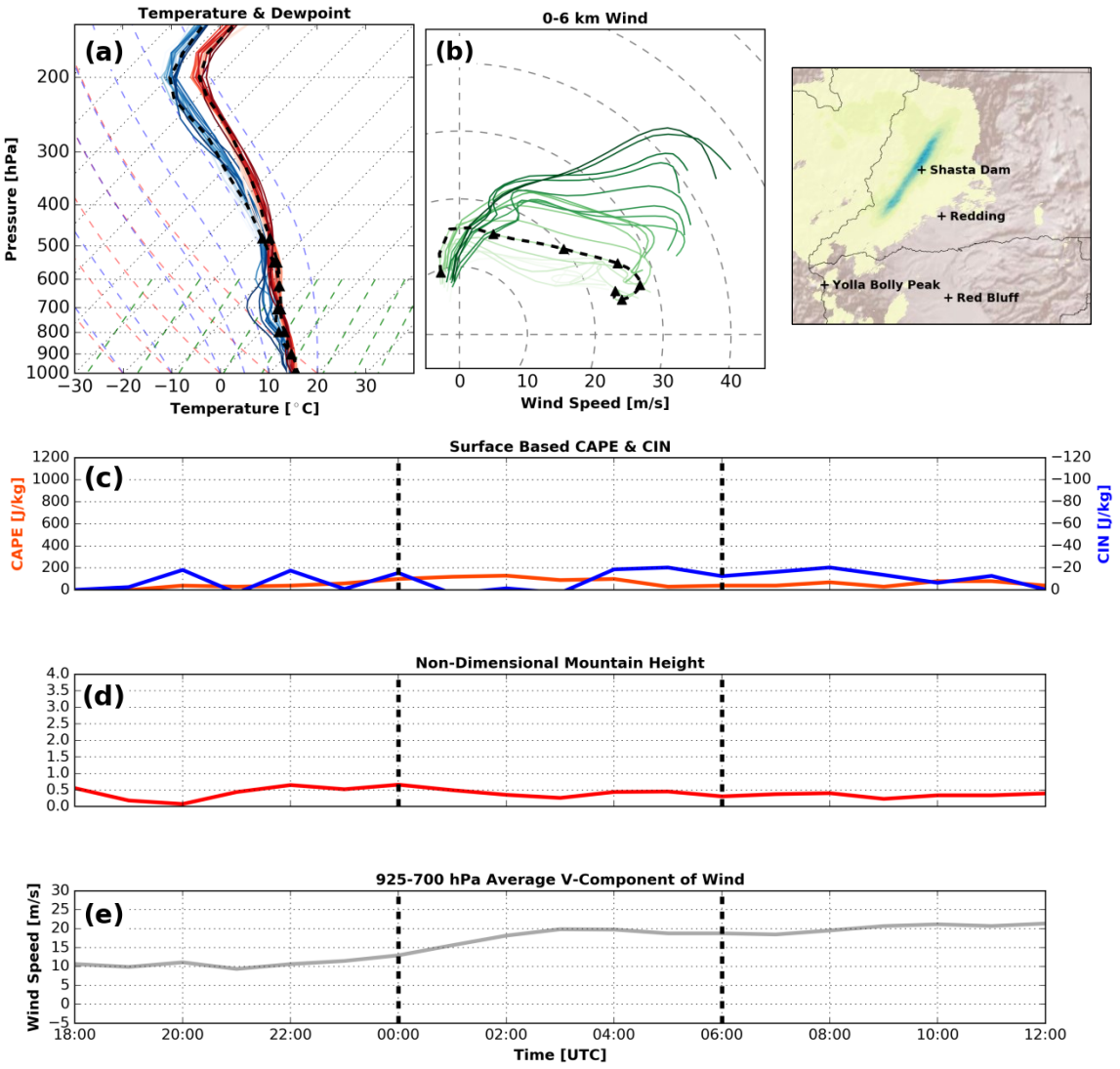

Fig. 21. RAP derived vertical profiles over Red Bluff of (a) temperature (°C, red) and dew point (°C, blue) and (b) winds from 0 to 6 km (m s^{-1}, green). Shading and black triangles as in Figure 20. RAP derived time series of (c) CAPE (J kg^{-1}, orange) and CIN (J kg^{-1}, blue), (d) non-dimensional mountain height (red) and (e) 925-700 hPa layer average meridional wind (m s^{-1}, grey). All parameters starting 6 hours prior to convective initiation (1800 UTC 8 February 2017) and ending 6 hours after cessation (1200 UTC 9 February 2017). Initiation and cessation times are indicated by black dashed lines in (c), (d) and (e). Event total precipitation in upper-right for reference.

c. 9 February 2017

Vertical temperature profiles on 9 February are distinct from those on 8 February; but somewhat similar, in terms of potential instability, to the14 October event (Fig. 20-21). Initially temperature and moisture profiles are similar to the 8 February case, with a moist adiabatic profile through the troposphere. However, as the event progresses, the 400-700 hPa layer experiences significant cooling and drying. For example, the dew point temperature decreases more than 20°C at 500 hPa, and temperatures cool ~5°C at 600 hPa between convective initiation and event cessation (Fig. 22a). During the closing hours of the event dry air descends into the lower troposphere (800-900 hPa), likely suppressing convection and ultimately contributing to event cessation.

The 9 February wind profile shows greater directional and speed shear in the lowest 2km than either the 14 October or 8 February events (Fig. 22b). At initiation the hodograph exhibits pronounced curvature due to southerly surface winds of ~10 m s^{-1} veering to southwest winds at 25-30 m s^{-1} at 2km. As the event progresses the hodograph becomes increasingly linear as surface winds diminish and upper levels winds shift slightly westward. By the time SCCZ convection dissipates, the hodograph closely resembles the 14 October hodograph (Fig. 20b) except with slightly less directional shear.

Surface-based CAPE and CIN begin similar to the 8 February case, with values near zero as a result of the moist adiabatic temperature profile (Fig. 22c). Later, the cooling in the 400-700 hPa layer destabilizes the mid-troposphere, thereby contributing to minimal but increasing CAPE of 100-200 J kg^{-1} by the end of the event. During this same period,

drying of the lower troposphere results in a significant increase in CIN to nearly -60 J kg^{-1} by event cessation.

The non-dimensional mountain height and layer-averaged meridional winds initially resemble 8 February with winds near 20 m s^{-1} (Fig. 22e) and unblocked flow (M<0.5; Fig. 22d). However, winds quickly decrease to 10-15 m s^{-1} by 0000 UTC coinciding with a slight rise in M to 0.5-1 for the remainder of the event. Meridional flow on 9 February was weaker than and slightly more blocked than flow on 8 February (Fig. 21d,e), but stronger than and less blocked than the 14 October event (Fig 20d,e). Radar observations are consistent with these findings, as convection on 9 February initiated along the upper Trinity Mountains then moved southeast over the lower Trinity Mountains (Fig. 13), resulting in a band location between the unblocked 8 February and blocked 14 October events.

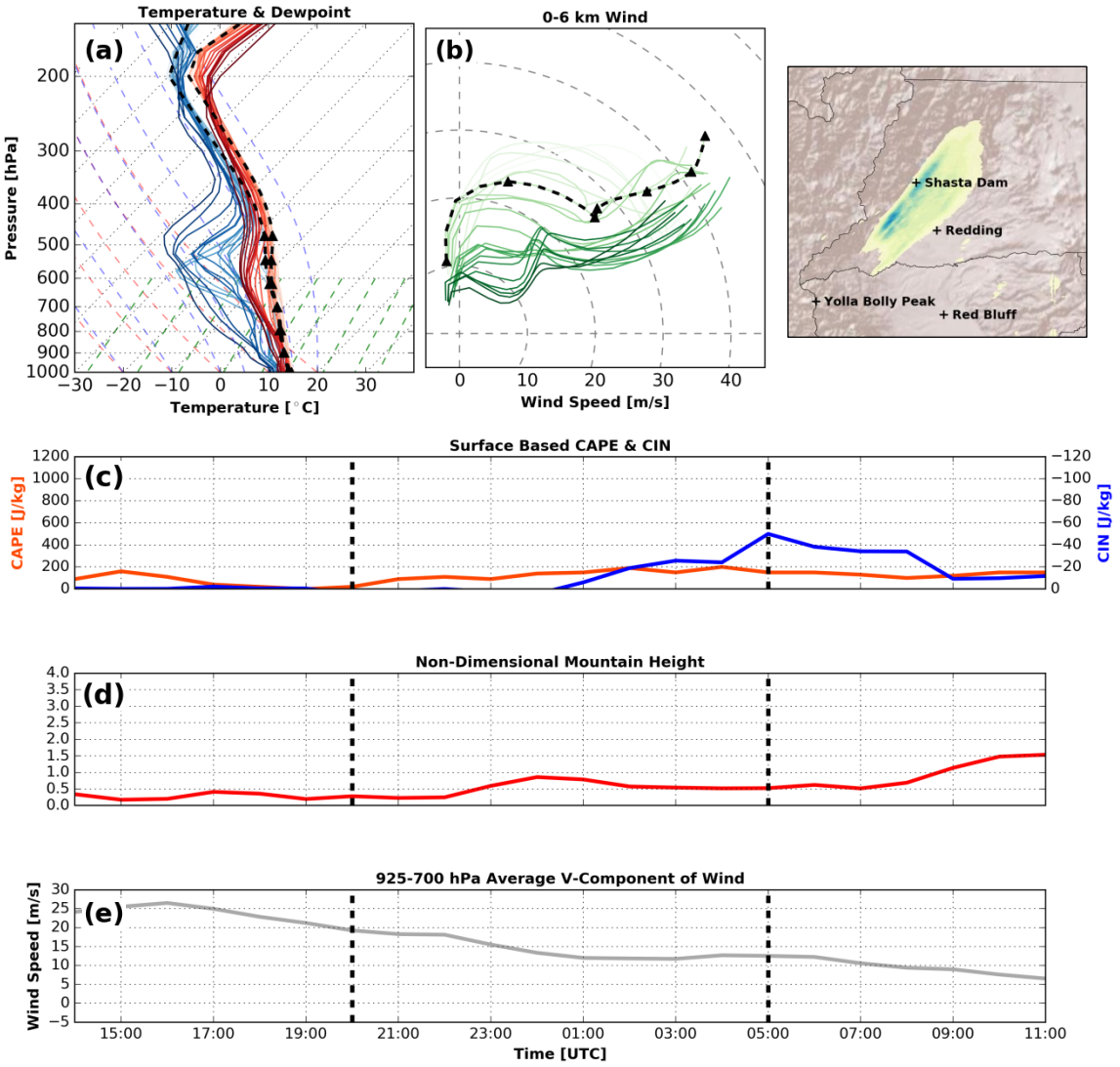

Fig. 22. RAP derived vertical profiles over Red Bluff of (a) temperature (°C, red) and dew point (°C, blue) and (b) winds from 0 to 6 km (m s^{-1}, green). Shading and black triangles as in Figure 20. RAP derived time series of (c) CAPE (J kg^{-1}, orange) and CIN (J kg^{-1}, blue), (d) non-dimensional mountain height (red) and (e) 925-700 hPa layer average meridional wind (m s^{-1}, grey). All parameters starting 6 hours prior to convective initiation (1400 UTC 9 February 2017) and ending 6 hours after cessation (1100 UTC 10 February 2017). Initiation and cessation times are indicated by black dashed lines in (c), (d) and (e). Event total precipitation in upper-right for reference.

d. 21 March 2017

Temperature, moisture and wind profiles on 21 March 2017 differ from the previous events. Specifically, the thermodynamic profiles are more favorable for surface based convection, with cold air aloft (0°C at ~2km) and warm surface temperatures of 12-20°C generating a steep lapse rate through the lower troposphere (Fig. 23a) . For comparison, the 14 October, 8 and 9 February events all featured a freezing level (0°C) much further aloft (3-4 km vs. 2 km in this case), with surface temperatures generally below 15-18°C, and thus a more stable lower troposphere. Substantial potential instability (theta-e decreasing with height) is further enhanced by the presence of dry air aloft (from 400-800 hPa) at the time of convective initiation (Fig. 23a). As a result of these factors, 21 March had higher CAPE values ($\geq$1000 J kg^{-1}, Fig. 23c) when compared to other SCCZ events ($\leq$500 J kg^{-1}, Fig. 20c, 21c, 22c, 24c). Interestingly, this suggests that there is more than one mode of convection initiation that contributes to SCCZ precipitation.

Winds during the 21 March event were also unique compared to other SCCZ events; most notably the lack of strong wind shear. Surface winds during initiation are southerly at ~10 m s^{-1} increasing to ~20 m s^{-1} and southwesterly at 3km (Fig. 23b), somewhat resembling conditions on 14 October (Fig. 20b). However upper level winds (3-6km) remain southwest at 20-30 m s^{-1} decreasing to 20-25 m s^{-1} by event cessation, resulting in significantly less shear than any previously discussed events. Compare, for example, the length of the hodograph in Fig. 23b and Fig. 20b.

Layer averaged meridional winds on 21 March were 15-20 m s^{-1} prior to event initiation, decreasing to 10-15 m s^{-1} around 1700 UTC and remaining relatively constant

through the remainder of the event (Fig. 23e). Meridional winds are weak compared to other events initiated over or northwest of the Trinity Mountains (8 and 9 February). In addition to weaker winds, flow on 21 March was more blocked than the 8 and 9 February, with M of 1-1.5 during the first half of the event decreasing to <1 by 2100 UTC and near 0.5 by event cessation (Fig. 23d). Interestingly, both meridional winds and blocking characteristics more closely resemble those of events susceptible to blocking (M>1; Fig. 20d, 22d), where convective bands were positioned over the lower Trinity Mountains; indicating flow blocking is likely overridden by other mechanisms.

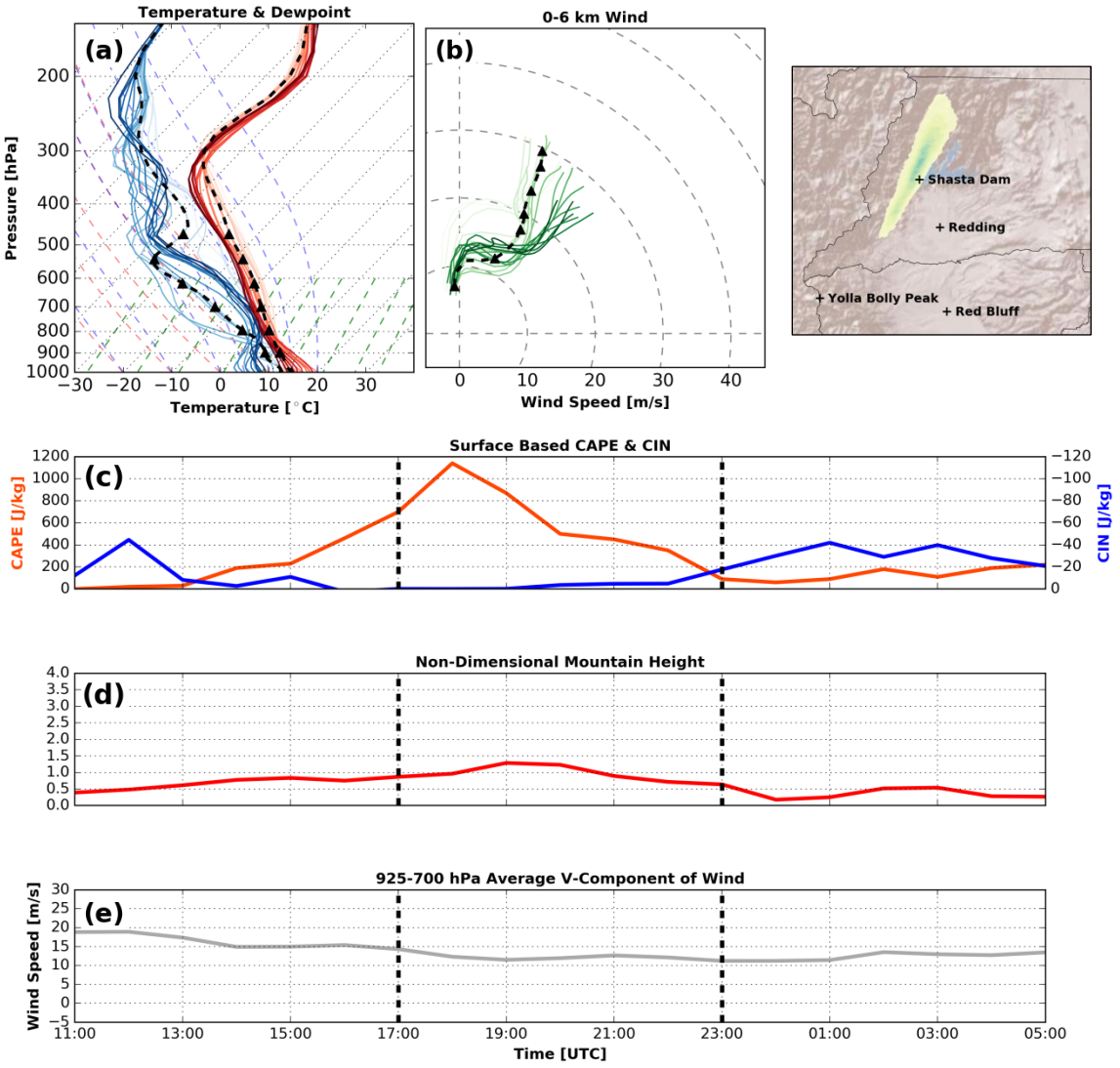

Fig. 23. RAP derived vertical profiles over Red Bluff of (a) temperature (°C, red) and dew point (°C, blue) and (b) winds from 0 to 6 km (m s^{-1}, green). Shading and black triangles as in Figure 20. RAP derived time series of (c) CAPE (J kg^{-1}, orange) and CIN (J kg^{-1}, blue), (d) non-dimensional mountain height (red) and (e) 925-700 hPa layer average meridional wind (m s^{-1}, grey). All parameters starting 6 hours prior to convective initiation (1100 UTC 21 March 2017) and ending 6 hours after cessation (0500 UTC 22 March 2017). Initiation and cessation times are indicated by black dashed lines in (c), (d) and (e). Event total precipitation in upper-right for reference.

e. 22 March 2017

Temperature and moisture profiles on 22 March are similar to 21 March, albeit with cooler temperatures throughout the profile (0°C isotherm just below 2 km; Fig. 24a). The moisture profiles show three distinct morphologies during the event. Prior to initiation (0700-1300 UTC) the humidity profiles indicate a moist neutral atmosphere. After 1300 UTC profiles become potentially unstable with a region of dry air around the 450-700 hPa layer. By event cessation the profiles show dissipation of the dry layer and a return to a moist profile, likely a result of the mesoscale convective system (MCS) that developed in the NSV on 22 March.

The 22 March hodograph shows weaker winds than on 21 March throughout the profile. However, 22 March has slightly more low level directional shear, with south-southeasterly surface winds of ~5 m s^{-1} veering to southwest at 10 m s^{-1} at 1 km (Fig. 24b). In contrast with previous events, 2-6 km winds remain <20 m s^{-1} for the majority of the event. Although significantly weaker, 22 March maintains a straight line hodograph from 2 to 6 km. After event cessation winds turn northerly as a result of the MCS induced outflow boundary that transited through the NSV after 2200 UTC (Fig. 17d).

The 22 March event initiated under low CAPE (<100 J kg^{-1}), moderate CIN (<-20 J kg^{-1}) conditions, again suggesting thermal mechanisms are not integral to SCCZ development (Fig. 24c). Although SCCZ convection initiated under low CAPE conditions, daytime heating developed modest CAPE (400-450 J kg^{-1}) and zero CIN by 2000 UTC. This instability combined with weakening wind shear likely contributed to the widespread diurnal convection that developed across the NSV on 22 March (Fig. 17).

Convection then organized into an MCS which ultimately began overwhelming the southerly flow across the NSV after 0000 UTC (Figs. 24b,e).

Compared to other events, the weak meridional flow on 22 March also resulted in significant flow blocking (M>1.5, Fig. 24d). Specifically, meridional winds remained less than 5 m s^{-1} throughout most of the event (Fig. 24e), allowing M to steadily increase from just ~0.5 at convective initiation to >2 by 1900 UTC (Fig. 24d). This increase coincides with the steady southward movement of the convective band from 1700 to 2200 UTC before it developed into a cold-pool dominated squall line and accelerated out of the region. The radar observed evolution and high values of M suggest that flow blocking may have played a role in the transition of the stationary band into a transient MCS.

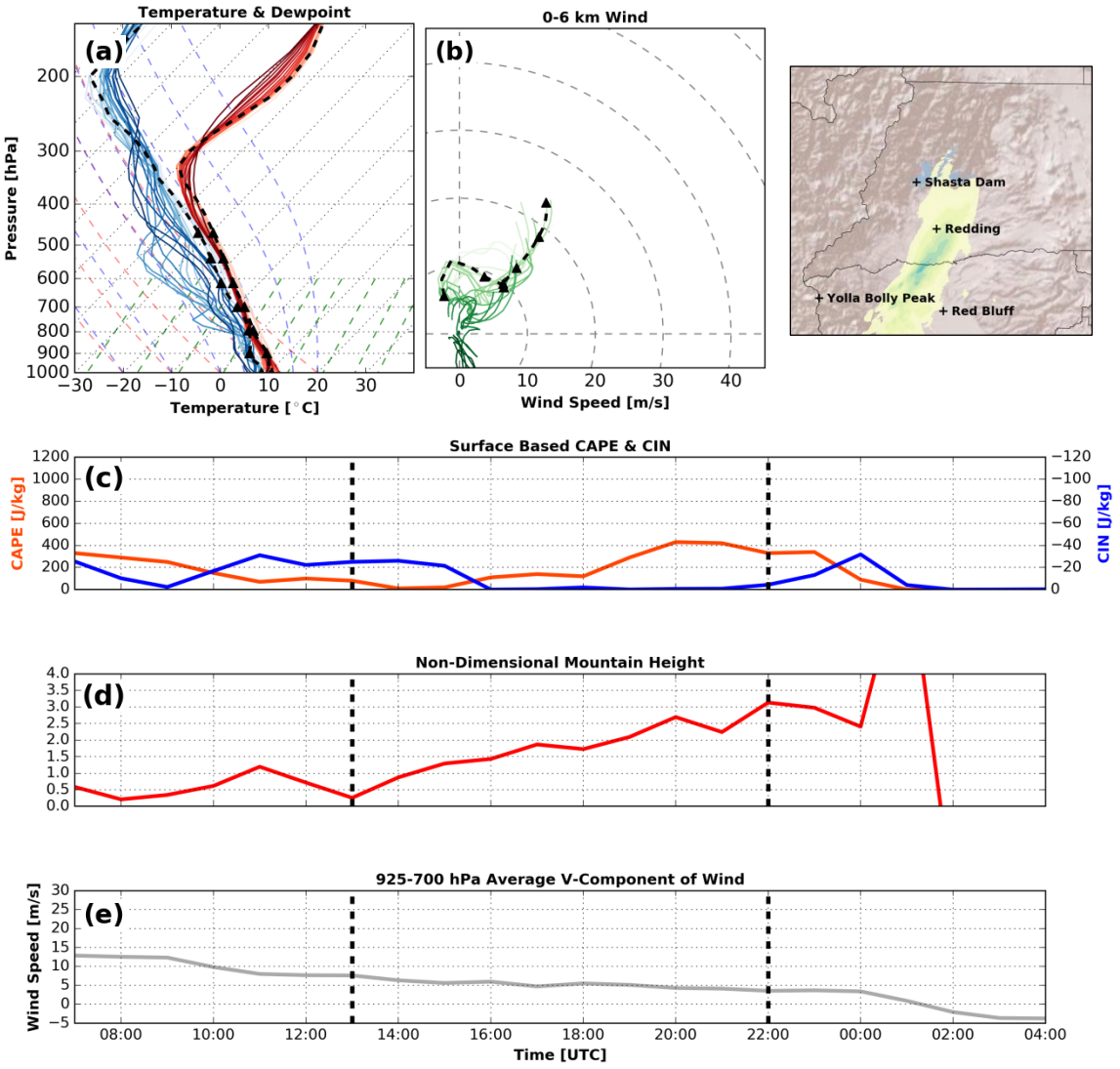

Fig. 24. RAP derived vertical profiles over Red Bluff of (a) temperature (°C, red) and dew point (°C, blue) and (b) winds from 0 to 6 km (m s^{-1}, green). Shading and black triangles as in Figure 20. RAP derived time series of (c) CAPE (J kg^{-1}, orange) and CIN (J kg^{-1}, blue), (d) non-dimensional mountain height (red) and (e) 925-700 hPa layer average meridional wind (m s^{-1}, grey). All parameters starting 6 hours prior to convective initiation (0700 UTC 22 March 2017) and ending 6 hours after cessation (0400 UTC 23 March 2017). Initiation and cessation times are indicated by black dashed lines in (c), (d) and (e). Event total precipitation in upper-right for reference.

f. Summary

RAP analyses indicate sensitivity of SCCZ morphology to the thermodynamic state of the atmosphere. Generally, well-developed SCCZ events occur in environments that support moist convection due to mechanical forcing (i.e., orographic ascent) and characterized by southerly near surface winds veering to southwest or west winds with height (Fig. 25). These veering winds generate either a clockwise-curving or a straight-line hodograph, both of which support linear convective organization. Within this broad categorization, we further delineate between events that have either:

1. Potential instability in the lower troposphere with moderate (15-25 m s^{-1}) or high 0-6 km shear (>25 m s^{-1})
2. Moist neutral stratification within the troposphere with moderate (15-25 m s^{-1}) or high 0-6 km shear (>25 m s^{-1})

Cases with moist neutral stratification can include convection embedded within stratiform precipitation, and are likely to occur over the terrain (unblocked), whereas cases with potential instability are likely to form isolated convection either over or off of the terrain. Within these environments the finer details of convective line orientation, linearity, and movement are sensitive to flow blocking, strength and direction of wind shear and strength of low level up valley flow, some of the details of which are explored in numerical simulations in following sections.

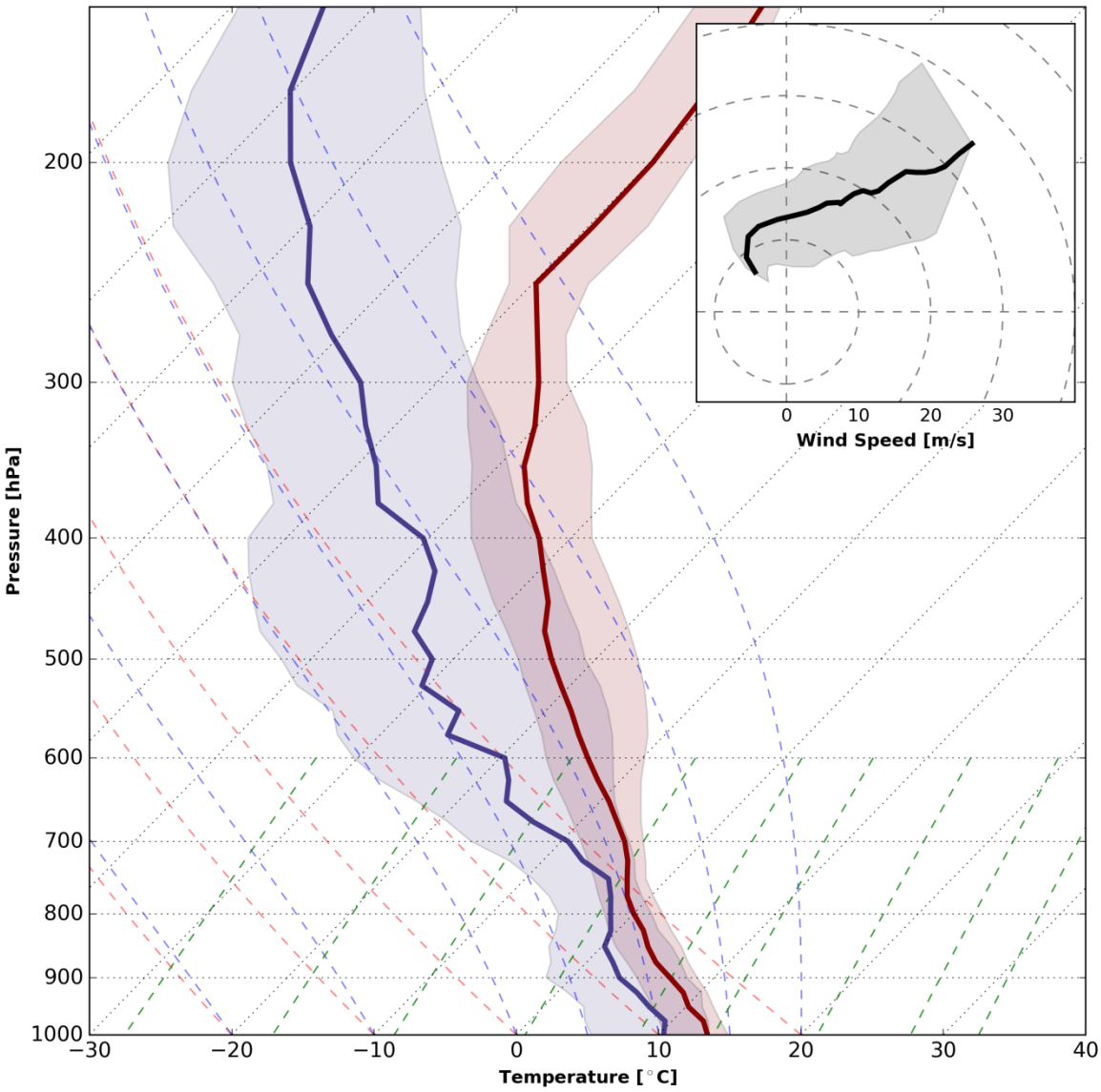

Fig. 25. Median (lines) and interquartile range (shaded) of RAP derived temperature (°C, red) and dew point (°C, blue) vertical profiles, and 0-6 km hodograph (inset, black) over Red Bluff at SCCZ convective initiation for all events.

4.3 Event WRF Analyses

Retrospective WRF simulations of selected SCCZ events were conducted to provide higher time-space resolution of the mechanisms controlling SCCZ convection than is available from the RAP analyses. Each event is simulated in full, but the analysis focuses on sub-periods of quasi-stationary, linear convection (1620-1820 UTC 14 October 2016, 0450-0600 UTC and 2250-2350 UTC 9 February 2017). For each sub-period, time averaged fields are used to probe the forcing mechanisms for convective initiation. Among the variables examined are terrain normal (with respect to the Trinity Mountains) and terrain parallel cross-sections of wind, potential temperature and reflectivity, vertical profiles of planar winds, potential temperature and equivalent potential temperature and plan view simulated radar reflectivity, vorticity, winds and surface convergence.

a. 14 October 2016

The time-mean simulated radar reflectivity for 14 October (1620-1820 UTC) indicates multiple linear convective features, including a pronounced SCCZ, forming across the mountains of Trinity, Siskiyou and Shasta Counties (Fig. 26a). The SCCZ convection initiates southwest of Redding and is stronger (40-50 dBZ) than adjacent bands (15-35 dBZ). The SCCZ band is oriented from southwest to northeast, paralleling the Trinity Mountains and the 1-3 km mean vector wind (Fig. 27e). Despite differences between the observed (Fig. 9) and simulated radar reflectivity, the model fields clearly indicated that WRF is capable of simulating quasi-stationary linear convection within the SCCZ.

Figure 26b shows the relative vorticity and wind at 500 meter above ground level (AGL). At this level there is a 7-10 m s^{-1} southerly flow over the NSV and southwesterly flow of 10-15 m s^{-1} across the Trinity Alps, Trinity Mountains and Yolla Bollys (Fig. 26b). Figure 26b also shows numerous shear induced vorticity bands, including downstream of topographic features, indicating terrain channeling of the southwest flow and favorability for linearly organized, low level, flow parallel convection across the region (Kirshbaum et. al 2007).

While there are numerous flow-parallel vorticity features in Fig. 26b, only one is linked to strong near-surface convergence: namely the SCCZ (Fig. 26c). Specifically, pronounced convergence in the lee of the Yolla Bollys and extending northeastward along the lower Trinity Mountains south of Shasta Dam corresponds with the region of high simulated radar reflectivity (Fig. 26a). The convergence occurs where the terrain channeled southerly flow in the NSV intersects the southwesterly flow over the higher terrain (Fig. 26b, c). Notably most of the other convergence features in the domain form in cross-wind, short, linear segments that are associated with local topographic features.

Terrain normal cross sections and upstream profiles are presented in Figure 27a and 27d, respectively. These data show a strong (15-20 m s^{-1}) low level jet advecting a shallow (200-300 m) layer of moist (mixing ratio of ~10 g kg^{-1}) but stable air (see theta profile in Fig. 27c) along a trajectory perpendicular to the Trinity Mountains. The nose of the jet impinges on the Trinity Mountains at ~500 m MSL, coinciding with the location of the simulated convective initiation (as apparent from the radar reflectivity in the cross section). Above the low level jet a broad area of moist instability (red contours shows

where theta-e decreases with height) is present from 500-3000 m MSL (Fig. 27a, c). The depth of the convection roughly corresponds to the depth of the potentially unstable layer.

The terrain parallel cross sections in Figure 27b reveal strong (25-35 m s^{-1}) plane-parallel flow at 3-4 km MSL, with low amplitude mountain waves in the lee of the Yolla Bollys. At the surface, winds are relatively calm in the lee of the Yolla Bollys, developing the region of increased cyclonic vorticity seen in Figure 26b.

The results of this simulation suggest that the convective initiation is dominated by orographic lifting very near the surface (500 m MSL) along the low angle slopes before the flow interacts with the higher terrain to the north. The lifting of the moist, potentially unstable air triggers convection that is then organized along the mean-wind vector, which is shown as a white arrow in Fig. 27e.

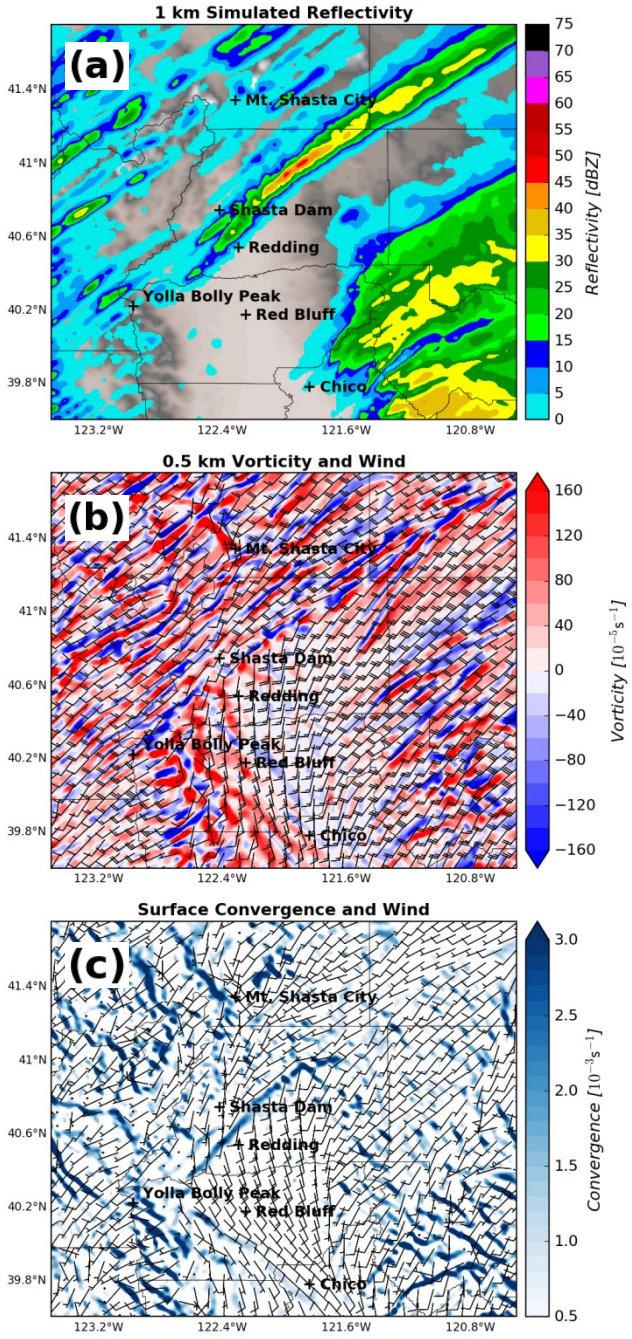

Fig. 26. WRF time averaged plan view of (a) 1 km reflectivity (shaded, dBZ), (b) 0.5 km vorticity (shaded, s^{-1}) and winds (as in Fig. 3), 10m convergence (shaded, s^{-1}) and winds (as in Fig. 3) from 1620 UTC to 1820 UTC on 14 October 2016.

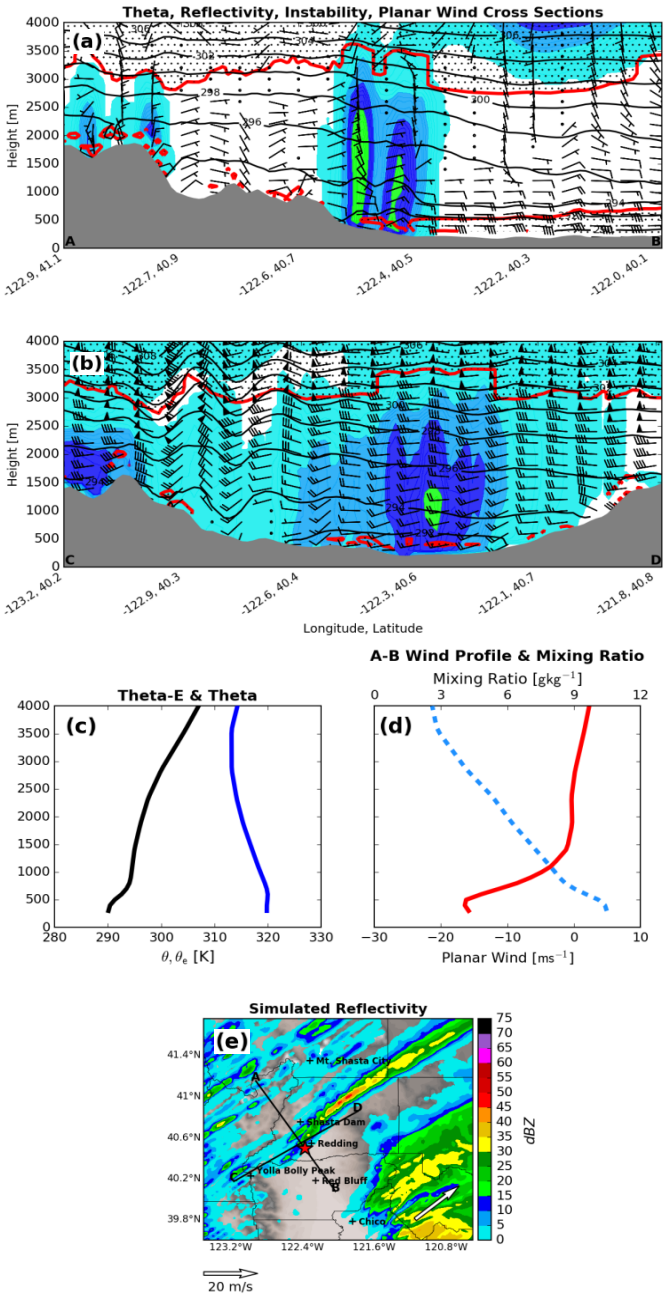

Fig. 27. WRF time averaged cross sections of reflectivity (shaded, dBZ), theta (contoured, K), $d\theta_e/dz>0$ (red contour, black hatching), and planar winds (as in Fig. 3) from points (a) A to B and (b) C to D shown in (e). Time averaged vertical profiles of (c) θ (solid black, K) and θ_e (solid blue, K), (d) water vapor mixing ratio (dashed light blue, g kg^{-1}) and AB planar wind profile (solid red, m s^{-1}) at red star in (e). Time averaged (e) reflectivity (shaded, dBZ), 1-3 km layer mean wind (white vector, m s^{-1}), and cross section and profile locations. Times averaged from 1620 UTC to 1820 UTC on 14 October 2016.

b. 8 February 2017

Figure 28 presents the time averaged plan-view summary of the simulated SCCZ convection for 0450-0600 UTC on 9 February. The radar reflectivity indicates widespread precipitation over the mountains of northern California with an embedded southwest-northeast oriented band of high (40-50 dbZ) reflectivity originating from a location west of Shasta Dam. This simulated reflectivity field is consistent with the radar observations of a linear convective band embedded in stratiform rain, as shown in Figure 11. One notable difference is presence of numerous simulated wind-parallel convective bands over the Sierra Nevada foothills southeast of Redding, which are not apparent in the radar observations, though that region is subject to KBBX beam blockage by the terrain.

As in the 14 October case numerous wind-parallel bands of positive and negative vorticity are apparent throughout the domain (Fig. 28b). However, once again, only one of the vorticity bands is coincident with an elongated region of near-surface convergence. Specifically, a strip of high convergence is apparent emanating from the immediate lee of the Yolla Bollys and extending to the north-northeast (Fig. 28c). The northern portions of the convergence line lose some of their linearity, taking on a more cellular structure. This strip of high convergence is once again distinct from the many cross wind convergence zones throughout the domain and is linked to a coherent boundary between the southerly flow in the valley and the southwesterly flow over the terrain. This confluent region is apparent in both Figures 28b and c.

The convergence line and location of convective initiation is also apparent in the terrain normal cross section (Fig. 29a). Compared to the 14 October case a stronger (20-25 m s^{-1} vs. 15-20 m s^{-1}) and deeper (~1 km vs. 0.5 km) low level jet is present. The nose of the jet is situated at a higher altitude than the 14 October event, with the highest winds near 750 m MSL (Fig. 29d). The higher altitude wind maximum corresponds to vigorous orographic ascent over the Trinity Mountains at a higher elevation than 14 October, and is closely linked to the reflectivity maximum apparent in the cross section (Fig. 29a). This finding, and the comparison with the 14 October case, strongly suggests that the height of the nose of the low level terrain normal jet influences the location of the convective initiation.

Additionally, the deeper jet advects a deeper moist layer (~9 g kg^{-1} at 1 km) over the Trinity Mountains and into the Trinity Alps, embedding SCCZ convection in a region of stratiform orographic precipitation (Fig. 29a, d). We also note that as in the 14 October case a statically stable layer is present below the jet nose (black line Fig. 29c). Kirshbaum and Durran (2005b) noted the importance of these orographically lifted stable layers in organizing linear convective bands. Also similar to 14 October, convection on 8 February is also oriented roughly along the 1-3 km layer mean wind (Fig. 29e).

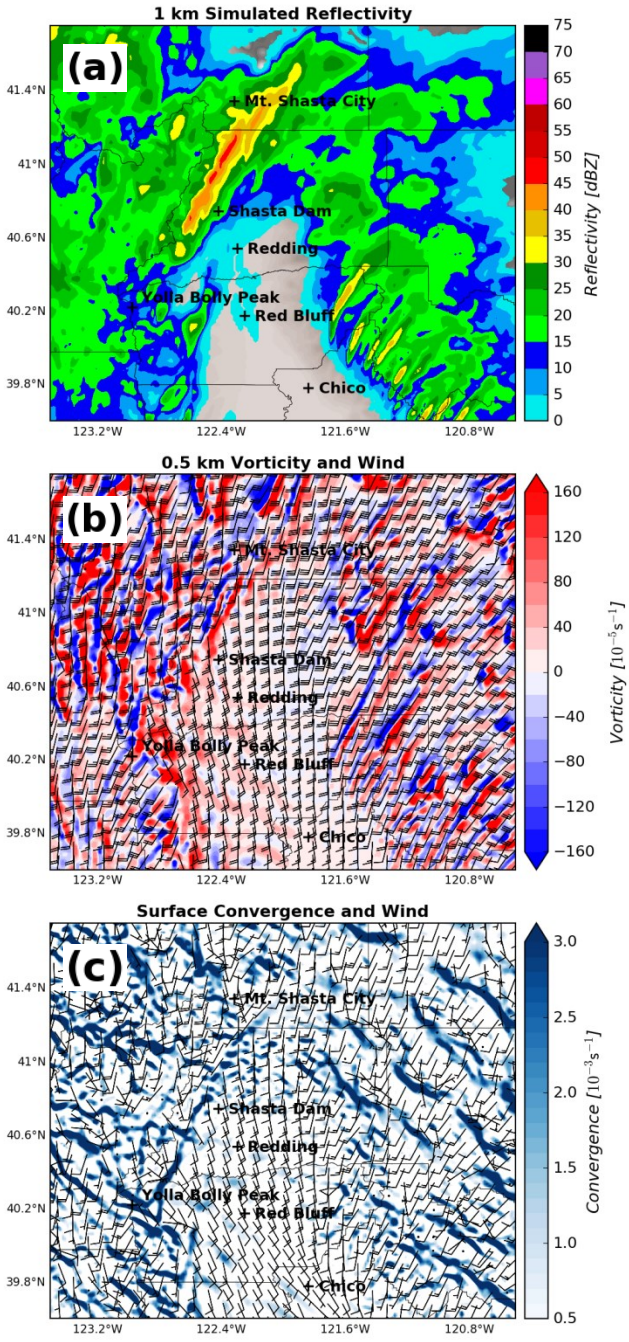

Fig. 28. WRF time averaged plan view of (a) 1 km reflectivity (shaded, dBZ), (b) 0.5 km vorticity (shaded, s^{-1}) and winds (as in Fig. 3), 10m convergence (shaded, s^{-1}) and winds (as in Fig. 3) from 0450 UTC to 0600 UTC on 9 February 2017.

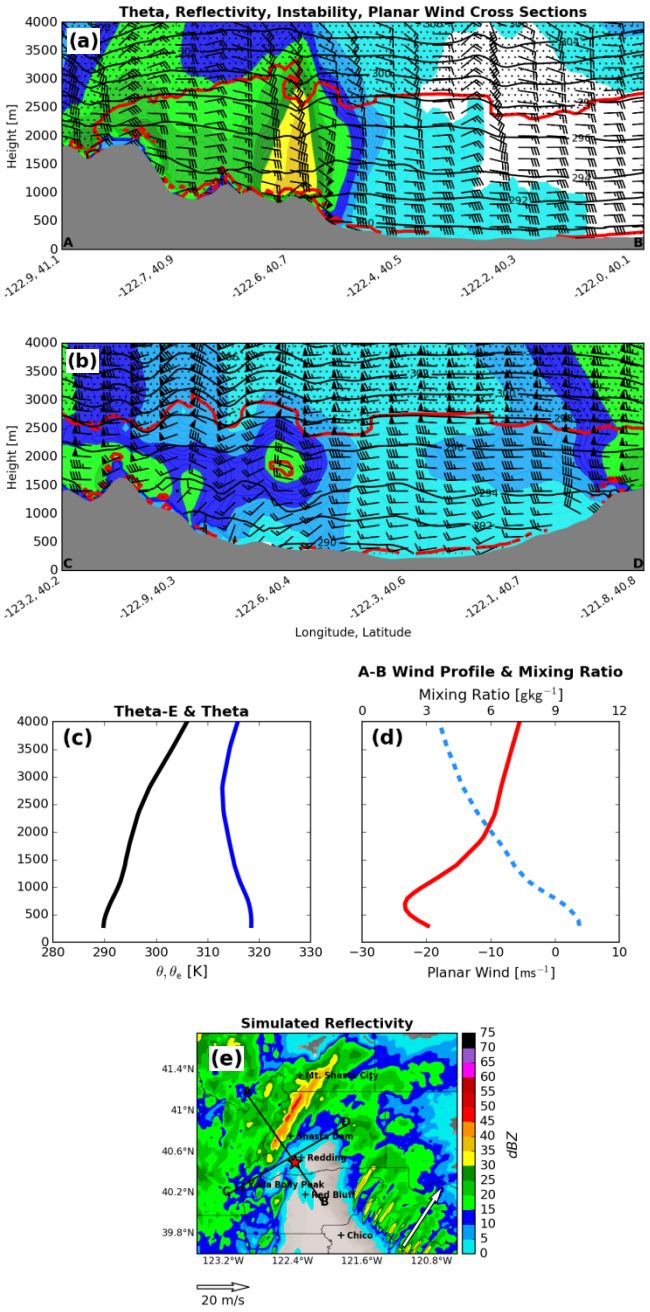

Fig. 29. WRF time averaged cross sections of reflectivity (shaded, dBZ), theta (contoured, K), $d\theta_e/dz>0$ (red contour, black hatching), and planar winds (as in Fig. 3) from points (a) A to B and (b) C to D shown in (e). Time averaged vertical profiles of (c) θ (solid black, K) and θ_e (solid blue, K), (d) water vapor mixing ratio (dashed light blue, g kg^{-1}) and AB planar wind profile (solid red, m s^{-1}) at red star in (e). Time averaged (e) reflectivity (shaded, dBZ), 1-3 km layer mean wind (white vector, m s^{-1}), and cross section and profile locations. Times averaged from 0450 UTC to 0600 UTC on 9 February 2017.

c. 9 February 2017

The 9 February simulation displays the most clearly defined linear SCCZ band of the three simulations, with convection initiating along the southern Shasta County line forming a discrete linear band through southeast Siskiyou County (Fig. 30a). Similar to previously simulations, the band is oriented with both the 1-3 km mean flow vector (Fig. 31e) and along the spine of the Trinity Mountains, with the mean wind and vorticity fields resembling those on 14 October. Notably, both cases feature terrain channeled southwest flow of 7.5-12.5 m s^{-1} along the Trinity Alps forming a pronounced wind shift boundary and opposing cyclonic-anti cyclonic vorticity bands over the Trinity Mountains (Fig. 30b). The bands extend well downstream of the topography and across Shasta County. As in both previous simulations the only elongated convergence feature is the convergence associated with the SCCZ, whereas most other convergence is oriented in across flow segments. The SCCZ convergence again forms where the southerly flow in the NSV (5-7.5 m s^{-1}) meets the weaker southwest winds along the Trinity Mountains (Fig. 30c).

The terrain normal cross sections on 9 February 2250-2350 UTC show a distinct convective band positioned over the lower Trinity Mountains (Fig. 31a). The 9 February 2250-2350 UTC event features deeper moist instability (~3.5 km) over the NSV and similar ridgetop winds (~25-30 m s^{-1}) as 9 February 0450-0600 UTC. Similar to the 14 October simulation, there is a shallow (~500 m AGL) ~20 m s^{-1} jet and associated 9-10 g kg^{-1} mixing ratio maximum. Similar to other events, the low level jet nose coincides with the elevation of convective initiation, leading to convective initiation over the lower

Trinity Mountains during the 9 February 2250-2350 simulation. Also similar to previous events, the 1-3 km mean flow vector is aligned with the convective band (Fig. 31e).

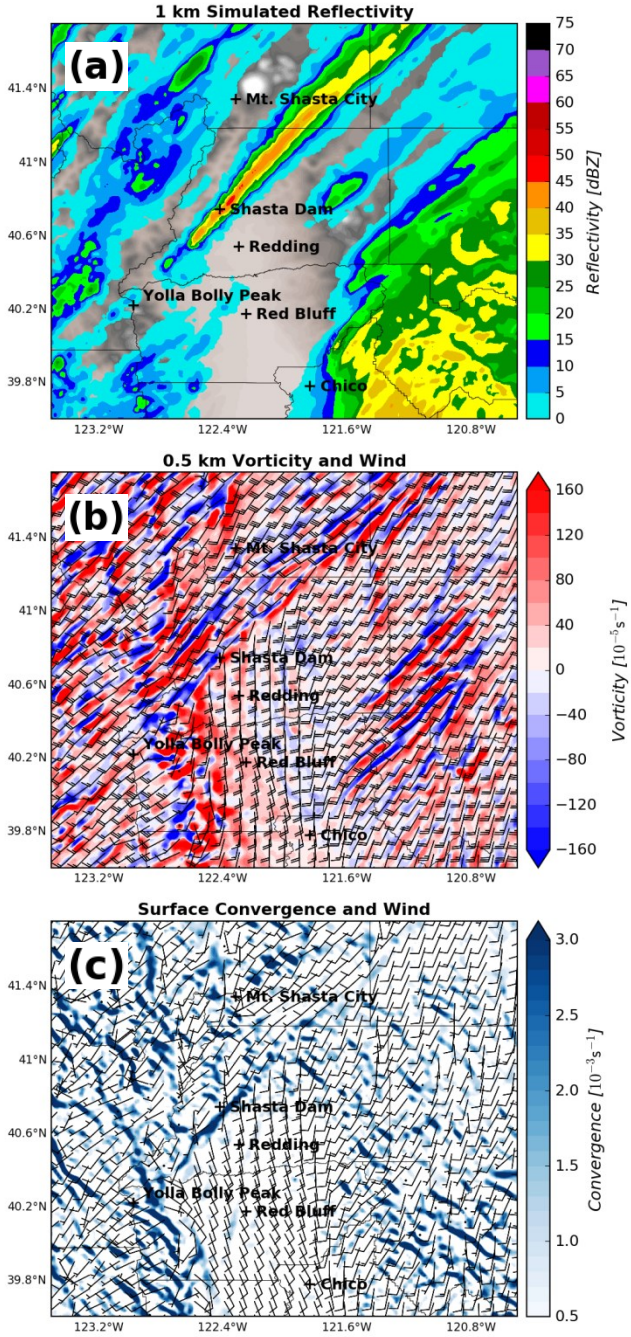

Fig. 30. WRF time averaged plan view of (a) 1 km reflectivity (shaded, dBZ), (b) 0.5 km vorticity (shaded, s^{-1}) and winds (as in Fig. 3), 10m convergence (shaded, s^{-1}) and winds (as in Fig. 3) from 2250 UTC to 2350 UTC on 9 February 2017.

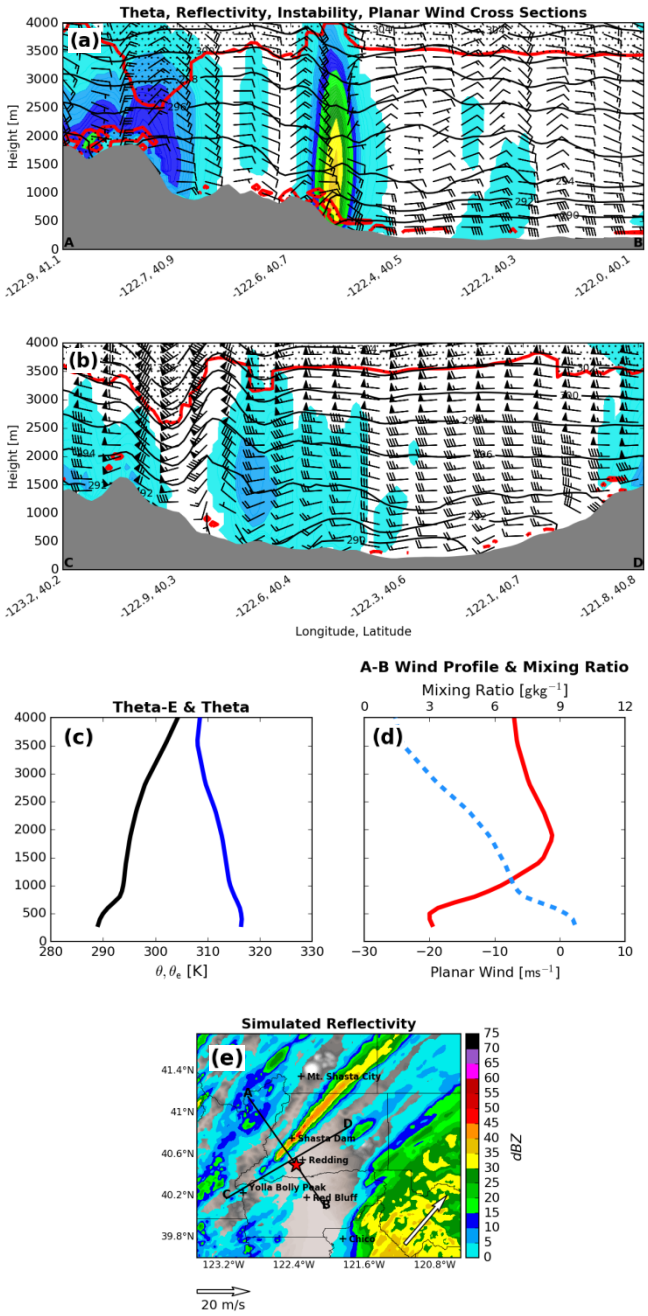

Fig. 31. WRF time averaged cross sections of reflectivity (shaded, dBZ), theta (contoured, K), $d\theta_e/dz>0$ (red contour, black hatching), and planar winds (as in Fig. 3) from points (a) A to B and (b) C to D shown in (e). Time averaged vertical profiles of (c) θ (solid black, K) and θ_e (solid blue, K), (d) water vapor mixing ratio (dashed light blue, g kg^{-1}) and AB planar wind profile (solid red, m s^{-1}) at red star in (e). Time averaged (e) reflectivity (shaded, dBZ), 1-3 km layer mean wind (white vector, m s^{-1}), and cross section and profile locations. Times averaged from 2250 UTC to 2350 UTC on 9 February 2017.

d. Summary

Each simulated case exhibits a pronounced low-level terrain normal jet. Although the depth and strength of the jet varies from case to case, the nose of the jet exerts a control on the location of convective initiation in the SCCZ for two reasons. First, the nose of the jet contains the strongest slope normal flow, thus coinciding with strong orographic ascent where the jet intersects topography. Second, the altitude of the jet nose is closely linked to the height at which the ambient upstream profile becomes potentially unstable. Specifically, statically stable yet very moist flow coupled with strong southerly flow (terrain normal winds of 18-25 m s^{-1}) within the LLJ advects high mixing ratio (9-12 g kg^{-1}) air up the NSV and into the Trinity Mountains. This moist but stable layer underlies drier and less statically stable air. Therefore, convection triggers near the interface of the LLJ and overlying air mass where the profile becomes potentially unstable and there is strong orographic ascent. Thus, a potentially important forecasting tool for distinguishing between individual SCCZ events initiation locations is the height of the LLJ maximum in the NSV, as this closely correlates with the elevation at which convective initiation occurs in the Trinity Mountains.

The simulations also reveal that the orientation of the SCCZ closely aligns with the layer-mean wind in each of the simulated cases. This is consistent with the findings in Miniscloux et al. (2001) and Kirshbaum and Durran (2005a) that linear convection organizes parallel to the mean wind vector.

Based on these results we concluded that in the future it should be possible to predict the orientation and initiation location of the SCCZ provided that forecast models can capture the structure of the low level jet and the wind profile in the NSV.

5. Conclusions and Future Work

Observational and radar analyses paired with numerical simulations indicate that a number of synoptic and mesoscale factors control the initiation and organization of SCCZ convection. These findings are summarized as follows:

a) Background Synoptic Requirements

Synoptic factors necessary to initiate SCCZ convection include: (1) a deepening 500-hPa trough northwest of California, with broad west-southwesterly flow aloft extending into Northern California (Fig. 3), (2) widespread high relative humidity aloft (700 hPa, Fig. 4), strong pressure-channeled, ageostrophic, near surface southerly flow in the NSV below 850-hPa linked to the development of the Sierra Barrier Jet (Fig. 5), and a pronounced lee side trough and windward ridge in the lee of the Coast Ranges and over the Sierra Nevada, respectively (Fig. 6).

This flow configuration generates a region of confluence and convergence at the northern terminus of the NSV that supports SCCZ convection. The location of 500-hPa trough and jet exit region generally supports synoptic lift, air mass destabilization, and the moisture necessary to initiate orographic convection across northern California. Although the influence of specific synoptic factors varies from case to case, their combined forcing provides a background environment favorable for SCCZ convection.

However, the specifics of the convection are determined by mesoscale processes described below.

b) Mesoscale Processes Dictating Convective Line Location

The mesoscale thermodynamics and flow-topography interactions across the NSV are ultimately responsible for initiating SCCZ convective events. Fundamental mesoscale components of SCCZ initiation include: (1) northward advection of high mixing ratio air by strong southerly winds up the NSV in the lowest 1 km AGL, (2) channeling of west southwest flow aloft by the Coast Ranges and Yolla Bollys, leading to leeside surface convergence on the western and northern periphery of the NSV and (3) altitude and strength of the low level jet maximum over the NSV.

Strong low-level flux of 9-12 g kg^{-1} mixing ratios provides ample moisture for sustaining convection in the SCCZ as the shallow moist layer is lifted by the Trinity Mountains release instability aloft. The interface between this shallow, stable moist layer within the LLJ, and the potentially unstable air aloft tends to dictate the elevation at which strong orographic ascent initiates convection (i.e. along the Trinity Mountains). While the height of the jet determines the location of strong orographic ascent, it also corresponds to the point at which the theta-e profile decreases most rapidly with height. Below the jet nose the flow is moist, but statically stable, while above the jet nose the flow is drier and less stable (to near neutral). Thus as the surface flow is lifted by the terrain, it triggers convection. The depth of the convection is largely determined by the depth of the unstable layer.

Flow parallel vorticity bands coinciding with surface convergence bands also develop downstream of the Yolla Bollys as a result of terrain channeling of southwesterly flow aloft. This is similar to convection shown in Alcott and Steenburgh (2013), where organization of linear convection over the Great Salt Lake was aided by terrain channeled flow upstream of the region. Southerly flow within the LLJ orographically lifted by the Trinity Mountains and converging with southwesterly flow aloft, generates coincident linear surface convergence and vorticity bands in the lee of the Yolly Bollys over the NSV. SCCZ events characterized by weaker southerly flow in the NSV are often associated with more westerly component to the wind aloft, resulting in a clockwise rotation of the convective bands when compared with flows with stronger southerly components. In contrast, stronger southerly surface flow is associated with more southwesterly flow aloft, resulting in a counter-clockwise rotation of the convective bands. The latter case primarily occurs in pre-frontal environments where deep layer strong southerly flow precedes a cold frontal passage; however both cases can significantly shift locations of precipitation maxima.

c) Dominant Factors Governing SCCZ Linearity and Duration

Although the southwest to northeast orientation of the Trinity Mountains likely reinforces linearity of SCCZ convection along a similar axis, the dominant mechanisms appear to be the depth, strength and direction of the low level wind shear over the NSV. Generally SCCZ convection can be categorized into two different low level shear environments: (1) southwesterly oriented and (2) westerly oriented 0-6 km shear and 1-3 km mean flow vectors. Subtle changes in these parameters results in significant changes

in linear convective structure, movement, orientation and location of associated precipitation maxima.

Southwesterly oriented 0-6 km shear vectors are evident in the highly linear 8 and 9 February and 21 March events (Fig. 21b, 22b, 23b). As deepening Pacific troughs approach the west coast, southwesterly flow aloft increases over northern California, while a deepening surface trough develops in the lee of the Coast Ranges. The result of the windward Sierra ridge coupled with a deepening lee trough is strong southerly flow in the NSV veering to southwesterly flow 1-2 km AGL. As both the 0-6 km shear vector and mean 1-3 km flow are both southwesterly, convection in these cases develops into both shear and flow parallel bands over the topography coinciding with the elevation of the low level jet maximum. Due to the relatively deep southerly flow in these cases, convective initiation occurs at a higher elevation on the slopes of the Trinity Mountains west of Shasta Lake (Fig. 11; 13; 15).

More westerly oriented 0-6 km shear vectors can be seen in 14 October event. As a result, convection on 14 October exhibited a more west-east oriented band when compared with 8 and 9 February and 21 March events. Although convective structure was altered by the change in upper level flow, convection still persisted for as long as southerly surface flow in the NSV impinged on the lower Trinity Mountains west of Redding. This would suggest that as long as strong southerly flow in the NSV is coupled with southwesterly to westerly 0-6 km shear and adequate low level moisture advection, convection will initiate in the SCCZ.

d) Summary and Future Work

It is clear an abundance of factors are needed to sustain linear SCCZ convective events. First, the background synoptic environment needs to be generally conducive to linear convection, including a veering low level wind profile with modest west or southwest flow at 500 hPa, mid and low level moisture and instability associated with a 500 hPa trough situated offshore of northern California. Secondly, a low level jet develops over the NSV advecting high mixing ratio air up the NSV and into the Trinity Mountains where it experiences orographic lift. Coinciding with the development of this low level jet, topographic channeling of the westerly and southwesterly flow aloft by the Coast Ranges and Yolla Bolly Mountains induces surface convergent bands downstream of the topography coincident with orographic lift of the LLJ by the Trinity Mountains. Further research using trajectory modeling and more expansive surface observation networks could better elucidate the exact interaction between terrain channeled flow and the NSV low level jet; however it is clear both mechanisms are critical in initiating and sustaining stationary SCCZ convection. Finally, strong low level wind shear across the NSV exhibited by straight-line or slightly curved hodographs organizes SCCZ convection into linear bands that align with both the 0-6 km shear vector as well as the mean 1-3 km flow field.

Other influences such as low level potential instability over the NSV, blocking effects of the Trinity Mountains and varying LLJ-topographic interactions also play roles in some SCCZ events. Although such influences are not always key components to SCCZ development they can subtly change event evolution and are subject to further research.

Future work in the NSV will need to address key limitations in the observation network over the region; namely sparse surface and upper air observation networks and beam blockage and bright-banding of KBBX radar returns over Shasta, Trinity and Siskiyou Counties. A field campaign using an expanded network of remote weather stations, mobile radars and wind profilers could greatly improve understanding of SCCZ events by supplementing the current observation network.

References

Alcott, T. I., and W. J. Steenburgh, 2013: Orographic Influences on a Great Salt Lake–Effect Snowstorm. *Mon. Weather Rev.*, **141**, 2432–2450, doi:10.1175/MWR-D-12-00328.1.

Anders, A. M., G. H. Roe, D. R. Durran, and J. R. Minder, 2007: Small-Scale Spatial Gradients in Climatological Precipitation on the Olympic Peninsula. *J. Hydrometeorol.*, **8**, 1068–1081, doi:10.1175/JHM610.1.

Andretta, T. A., and D. S. Hazen, 1998: Doppler Radar Analysis of a Snake River Plain Convergence Event. *Weather Forecast.*, **13**, 482–491, doi:10.1175/1520-0434(1998)013<0482:DRAOAS>2.0.CO;2.

Banta, R. M., 1990: The Role of Mountain Flows in Making Clouds. *Atmospheric Processes over Complex Terrain*, American Meteorological Society, Boston, MA, 229–283 http://link.springer.com/10.1007/978-1

Benjamin, S. G., and Coauthors, 2016: A North American Hourly Assimilation and Model Forecast Cycle: The Rapid Refresh. *Mon. Weather Rev.*, **144**, 1669–1694, doi:10.1175/MWR-D-15-0242.1.

Chen, F., and J. Dudhia, 2001: Coupling an Advanced Land Surface–Hydrology Model with the Penn State–NCAR MM5 Modeling System. Part I: Model Implementation and Sensitivity. *Mon. Weather Rev.*, **129**, 569–585, doi:10.1175/1520-0493(2001)129<0569:CAALSH>2.0.CO;2.

Cosma, S., E. Richard, and F. Miniscloux, 2002: The role of small-scale orographic features in the spatial distribution of precipitation. *Q. J. R. Meteorol. Soc.*, **128**, 75–92, doi:10.1256/00359000260498798.

Crum, T. D., and R. L. Alberty, 1993: The WSR-88D and the WSR-88D Operational Support Facility. *Bull. Am. Meteorol. Soc.*, **74**, 1669–1687, doi:10.1175/1520-0477(1993)074<1669:TWATWO>2.0.CO;2.

Durran, D. R., 1990: Mountain Waves and Downslope Winds. *Atmospheric Processes over Complex Terrain*, American Meteorological Society, Boston, MA, 59–81 http://link.springer.com/10.1007/978-1-935704-25

Graf, W. L., 2006: Downstream hydrologic and geomorphic effects of large dams on American rivers. *Geomorphology*, **79**, 336–360, doi:10.1016/J.GEOMORPH.2006.06.022.

Grossman, R. L., and D. R. Durran, 1984: Interaction of Low-Level Flow with the Western Ghat Mountains and Offshore Convection in the Summer Monsoon. *Mon. Weather Rev.*, **112**, 652–672, doi:10.1175/1520-0493(1984)112<0652:IOLLFW>2.0.CO;2.

Hagen, M., J. van Baelen, and E. Richard, 2011: Influence of the wind profile on the initiation of convection in mountainous terrain. *Q. J. R. Meteorol. Soc.*, **137**, 224–235, doi:10.1002/qj.784.

Hong, S.-Y., Y. Noh, and J. Dudhia, 2006: A New Vertical Diffusion Package with an Explicit Treatment of Entrainment Processes. *Mon. Weather Rev.*, **134**, 2318–2341, doi:10.1175/MWR3199.1.

Horel, J., and Coauthors, 2002: Mesowest: Cooperative Mesonets in the Western United States. *Bull. Am. Meteorol. Soc.*, **83**, 211–225, doi:10.1175/1520-0477(2002)083<0211:MCMITW>2.3.CO;2.

Houze, R. A., 1993: *Cloud dynamics*. Academic Press, Cambridge, MA, USA , 573 pp.

Houze, R. A., C. N. James, and S. Medina, 2001: Radar observations of precipitation and airflow on the Mediterranean side of the Alps: Autumn 1998 and 1999. *Q. J. R. Meteorol. Soc.*, **127**, 2537–2558, doi:10.1002/qj.49712757804.

Iacono, M. J., J. S. Delamere, E. J. Mlawer, M. W. Shephard, S. A. Clough, and W. D. Collins, 2008: Radiative forcing by long-lived greenhouse gases: Calculations with the AER radiative transfer models. *J. Geophys. Res.*, **113**, D13103, doi:10.1029/2008JD009944.

Jiang, Q., 2006: Precipitation over Concave Terrain. *J. Atmos. Sci.*, **63**, 2269–2288, doi:10.1175/JAS3761.1.

Kain, J. S., 2004: The Kain–Fritsch Convective Parameterization: An Update. *J. Appl. Meteorol.*, **43**, 170–181, doi:10.1175/1520-0450(2004)043<0170:TKCPAU>2.0.CO;2.

Kirshbaum, D. J., G. H. Bryan, R. Rotunno, and D. R. Durran, 2007: The Triggering of Orographic Rainbands by Small-Scale Topography. *J. Atmos. Sci.*, **64**, 1530–1549, doi:10.1175/JAS3924.1.

Kirshbaum, D. J., and D. R. Durran, 2004: Factors Governing Cellular Convection in Orographic Precipitation. *J. Atmos. Sci.*, **61**, 682–698, doi:10.1175/1520-0469(2004)061<0682:FGCCIO>2.0.CO;2.

Kirshbaum, D. J., and D. R. Durran, 2005: Observations and Modeling of Banded Orographic Convection. *J. Atmos. Sci.*, **62**, 1463–1479, doi:10.1175/JAS3417.1.

Kirshbaum, D. J., and D. R. Durran, 2005: Atmospheric Factors Governing Banded Orographic Convection. *J. Atmos. Sci.*, **62**, 3758–3774, doi:10.1175/JAS3568.1.

Kirshbaum, D., B. Adler, N. Kalthoff, C. Barthlott, and S. Serafin, 2018: Moist Orographic Convection: Physical Mechanisms and Links to Surface-Exchange Processes. *Atmosphere (Basel).*, **9**, 80, doi:10.3390/atmos9030080.

Hughes, M., P. J. Neiman, E. Sukovich, and M. Ralph, 2012: Representation of the Sierra Barrier Jet in 11 years of a high-resolution dynamical reanalysis downscaling compared with long-term wind profiler observations. *J. Geophys. Res. Atmos.*, **117**, n/a-n/a, doi:10.1029/2012JD017869.

Marshall, J. S., and W. McK. Palmer, 1948: The distribution of raindrops with size. *J. Meteor.*, **5**, 165–166, doi:10.1175/1520-0469(1948)005%3C0165:TDORWS%3E2.0.CO;2

Mass, C., 1981: Topographically Forced Convergence in Western Washington State. *Mon. Weather Rev.*, **109**, 1335–1347, doi:10.1175/1520-0493(1981)109<1335:TFCIWW>2.0.CO;2.

Mass, C. F., and D. P. Dempsey, 1985: A One-Level, Mesoscale Model for Diagnosing Surface Winds in Mountainous and Coastal Regions. *Mon. Weather Rev.*, **113**, 1211–1227, doi:10.1175/1520-0493(1985)113<1211:AOLMMF>2.0.CO;2.

Matrosov, S. Y., F. M. Ralph, P. J. Neiman, and A. B. White, 2014: Quantitative Assessment of Operational Weather Radar Rainfall Estimates over California's Northern Sonoma County Using HMT-West Data. *J. Hydrometeorol.*, **15**, 393–410, doi:10.1175/JHM-D-13-045.1.

Miniscloux, F., J. D. Creutin, and S. Anquetin, 2001: Geostatistical Analysis of Orographic Rainbands. *J. Appl. Meteorol.*, **40**, 1835–1854, doi:10.1175/1520-0450(2001)040<1835:GAOOR>2.0.CO;2.

Monteverdi, J. P., and J. Quadros, 1994: Convective and Rotational Parameters Associated with Three Tornado Episodes in Northern and Central California. *Weather Forecast.*, **9**, 285–300, doi:10.1175/1520-0434(1994)009<0285:CARPAW>2.0.CO;2.

Neiman, P. J., E. M. Sukovich, F. M. Ralph, and M. Hughes, 2010: A Seven-Year Wind Profiler–Based Climatology of the Windward Barrier Jet along California's Northern Sierra Nevada. *Mon. Weather Rev.*, **138**, 1206–1233, doi:10.1175/2009MWR3170.1.

Neiman, P. J., M. Hughes, B. J. Moore, F. M. Ralph, and E. M. Sukovich, 2013: Sierra Barrier Jets, Atmospheric Rivers, and Precipitation Characteristics in Northern California: A Composite Perspective Based on a Network of Wind Profilers. *Mon. Weather Rev.*, **141**, 4211–4233, doi:10.1175/MWR-D-13-00112.1.

Neiman, P. J., F. M. Ralph, B. J. Moore, and R. J. Zamora, 2014: The Regional Influence of an Intense Sierra Barrier Jet and Landfalling Atmospheric River on Orographic Precipitation in Northern California: A Case Study. *J. Hydrometeorol.*, **15**, 1419–1439, doi:10.1175/JHM-D-13-0183.1.

Office of the Federal Coordinator for Meteorology, 2016: *Federal Meteorological Handbook no. 11 - Doppler Radar Meteorological Observations (WSR-88D) Part A*. 15-16 pp.

Parish, T. R., 1982: Barrier Winds Along the Sierra Nevada Mountains. *J. Appl. Meteorol.*, **21**, 925–930, doi:10.1175/1520-0450(1982)021<0925:BWATSN>2.0.CO;2.

Ralph, F. M., J. M. Cordeira, P. J. Neiman, and M. Hughes, 2016: Landfalling Atmospheric Rivers, the Sierra Barrier Jet, and Extreme Daily Precipitation in Northern California's Upper Sacramento River Watershed. *J. Hydrometeorol.*, **17**, 1905–1914, doi:10.1175/JHM-D-15-0167.1.

Skamarock, C., B. Klemp, J. Dudhia, O. Gill, M. Barker, W. Wang, and G. Powers, 2005: *A Description of the Advanced Research WRF Version 2*. NCAR Technical Note NCAR/TN-468+STR, doi:10.5065/D6DZ069T.

Staudenmaier, M., 1995: *The 10 February 1994 Oroville Tornado A Case Study.* NOAA Technical Memorandum. NWS WR-229. 1-47 pp.

Tardy, A., 2002: *The Northern Sacramento Valley Surface Moisture Convergence Zone*. Western Region Technical Attachment. No. 02-07. Sacramento, CA, 1-17 pp.

Thompson, G., P. R. Field, R. M. Rasmussen, and W. D. Hall, 2008: Explicit Forecasts of Winter Precipitation Using an Improved Bulk Microphysics Scheme. Part II: Implementation of a New Snow Parameterization. *Mon. Weather Rev.*, **136**, 5095–5115, doi:10.1175/2008MWR2387.1.

Watson, C. D., and T. P. Lane, 2012: Sensitivities of Orographic Precipitation to Terrain Geometry and Upstream Conditions in Idealized Simulations. *J. Atmos. Sci.*, **69**, 1208–1231, doi:10.1175/JAS-D-11-0198.1.

Wesley, D. A., R. M. Rasmussen, and B. C. Bernstein, 1995: Snowfall Associated with a Terrain-Generated Convergence Zone during the Winter Icing and Storm Project. *Mon. Weather Rev.*, **123**, 2957–2977, doi:10.1175/1520-0493(1995)123<2957:SAWATG>2.0.CO;2.

Whiteman, C. D., and J. C. Doran, 1993: The Relationship between Overlying Synoptic-Scale Flows and Winds within a Valley. *J. Appl. Meteorol.*, **32**, 1669–1682, doi:10.1175/1520-0450(1993)032<1669:TRBOSS>2.0.CO;2.

Yoshizaki, M., and Coauthors, 2000: Analytical and Numerical Study of the 26 June 1998 Orographic Rainband Observed in Western Kyushu, Japan. *J. Meteorol. Soc. Japan. Ser. II*, **78**, 835–856, doi:10.2151/jmsj1965.78.6_835.